Processing of Aluminum Alloys Containing Displacement Reaction Products

Michael T. Stawovy

Dissertation submitted to the Faculty of the Virginia Polytechnic Institute and State University in partial fulfillment of the requirements for the degree of

Doctor of Philosophy
in
Materials Science & Engineering

Alex O. Aning, Chair
William Curtin
Stephen L. Kampe
William T. Reynolds
John A. Wert

July 15th, 1998
Blacksburg, Virginia

Keywords: Mechanical Alloying, Displacement Reactions, High Temperature Aluminum Alloys

Processing of Aluminum Alloys Containing Displacement Reaction Products

Michael T. Stawovy

(ABSTRACT)

Aluminum and metal-oxide powders were mixed using mechanical alloying. Exothermic displacement reactions could be initiated in the powders either by mechanical alloying alone or by heat treating the mechanically alloyed powders. Exponential relationships developed between the initiation time of the reaction and the mechanical alloying charge ratio. The exponential relationships were the result of changes in the intensity and quantity of collisions occurring during mechanical alloying. Differential thermal analysis of the mechanically alloyed powders indicated that increased milling time inhibited the initiation of the displacement reactions. It is believed that the reactions were inhibited because of heat dissipation from reacting oxide particles into the surrounding metal. Determining the effects of mechanical alloying on displacement reactions will lead to a more thorough understanding of the kinetics of mechanical alloying.

Reacted powders were densified by uniaxial compaction and extrusion. Metallographic analysis of the reacted specimens confirmed the findings of the thermal analysis. Increased mechanical alloying inhibited the chemical reactions. Densified specimens from longer-milled mechanically alloyed specimens showed finer, more uniformly dispersed reaction products. These samples also showed increased mechanical properties as a result of their finer microstructure. Current particle strengthening models were used to accurately predict room temperature properties. Because of the fine microstructures produced, it may be possible to use similar techniques to yield new high-temperature aluminum alloys.

Acknowledgements

I would like to start by thanking the person who convinced me to persevere to this level of education. Dr. Alex Aning was a key reason for my staying at Virginia Tech and completing my doctorate. He is not only my committee chairman, but more importantly, a close friend. He is an excellent motivator and will always be and inspiration to me.

I would also like to thank the rest of my committee. Drs. Bill Reynolds, Steve Kampe, Bill Curtin, and John Wert were gracious enough to endure my pathetic questions. They were also made themselves available to me at all times. For this, I am deeply indebted.

I thank my family for always being there for support and guidance.

I thank my numerous friends for alternative guidance.

Lastly, I thank my wife, Becky. She has had enduring patience during the completion of this work. She has sacrificed both time and personal comfort to allow me to finish my degree. Without her I am insignificant. She is my everything!

Table of Contents

List of Figures

List of Tables

Chapter 1 Introduction

Mechanical alloying (MA) has been employed for the production of various powder metallurgy alloys for over 25 years [1-2]. Over that period, however, limited work has been done to understand the mechanisms that occur during the process [3-7]. One issue of particular interest has been the kinetics of physical and chemical changes occurring during MA. By studying exothermic chemical reactions that occur during MA milling, it was possible to make advances in the understanding MA kinetics.

Chemical reactions that take place during MA have been termed mechanochemical reactions. Several different reactions have been documented in the literature to take place during MA [8-10]. Of these various types of reactions, probably the best understood are displacement reactions. A displacement reaction is a reaction in which a metal oxide (MO) is reduced by a reactive metal (R) to form the metal (M) and the reactive metal oxide (RO). These "thermite-type" reactions are exemplified by the reduction of Fe_2O_3 or SiO_2 by aluminum as described by equations 1 and 2.

$$2Al + Fe_2O_3 \rightarrow 2Fe + Al_2O_3 \tag{1.1}$$

$$4Al + 3SiO_2 \rightarrow 3Si + 2Al_2O_3 \tag{1.2}$$

In the current work, mixtures of aluminum and Fe_2O_3 or SiO_2 were produced using MA at various milling conditions. Displacement reactions were initiated by continued MA milling or post-MA heat treatments. Reaction initiation times during milling were determined by monitoring the presence of reaction products by x-ray diffraction. Using these reactions, it was possible to develop relationships between chemistry, MA milling time and MA charge ratio (a ratio of the mass of the milling media to the powder charge). Also, Differential Thermal Analysis (DTA) was used to monitor the reaction temperatures upon heating. This made it possible to determine if MA caused changes in the chemical reaction mechanisms by determining the apparent activation energies of the reactions. This work is a prelude to determining the energy that is imparted to the powder during MA. Determination of which is critical in understanding the kinetics of MA.

In parallel with studying the kinetics of MA, the same displacement reactions were applied as a means to dispersion strengthen aluminum. There has been an increased desire for high temperature aluminum alloys that could replace steel and titanium in applications in the 200°C - 400°C temperature range. Such high temperatures necessitate the use of dispersion strengthening as the primary strengthening mechanism. At high temperatures, dispersed ceramic or intermetallic particles are better able to inhibit the primary deformation mechanisms than precipitates. At those temperatures, precipitates tend to coarsen or dissolve into the matrix limiting their effectiveness compared to dispersoids, which are generally more stable [11].

Current dispersion strengthened alloys are usually produced using a powder metallurgy route such as mechanical alloying. The fracturing and welding that occur during MA create a fine and uniform dispersion by blending surface oxides or added oxides into the metal. In contrast to creating dispersoids by the addition of oxides, this study created dispersoids in-situ via chemical displacement reaction. Selection of the Al-Fe_2O_3 displacement reaction system for this initial work was important for two reasons. In addition to providing the most detailed background on displacement reactions, the Al-Fe_2O_3 system yields Al -Fe reaction products. The Al-Fe system is also the most widely studied system with regard to the production of high temperature aluminum alloys. Numerous studies have been performed on experimental and production alloys based on the Al-Fe system [12-13].

Mixtures of aluminum and Fe_2O_3 were produced using MA at several milling conditions. Following MA, exothermic displacement reactions were initiated by heat treatments. Reacted powders were analyzed for reaction product structure, particle size, and chemistry. The reacted powders were densified using uniaxial compaction or warm extrusion and the resulting material was analyzed for microstructure, chemistry, and room temperature mechanical properties. Because of the non-stoichiometric nature of the mixtures, there was an excess of Al present to react with the liberated Fe. Intermetallic phases, predominantly $Al_{13}Fe_4$, formed and provided particle strengthening along-side the

Al_2O_3 particles that also formed during the reaction. Based on the microstructural features, current material strengthening models were applied and compared to experimental values. Strengthening models indicate that the reaction products are responsible for providing increased strength at room temperature. Future efforts will include determination of the high temperature mechanical properties and assessing the viability of these alloys for high temperature alloy production.

1. J. S. Benjamin, Scientific American, 234, 5, 1976, pp. 40.
2. J. S. Benjamin, Metall. Trans., 5, 1974, pp. 1929.
3. R. M. Davis, B. McDermott, C. C. Koch, Metall. Trans., vol 19A, 1988, pp. 2867-2874.
4. D. R. Maurice,T. H. Courtney, Metall. Trans., 21A, 2, 1990, pp. 289-303.
5. D. R. Maurice,T. H. Courtney, Metall. Trans., vol. 25A, 1994, pp. 147-158.
6. G. B. Schaffer, P.G. McCormick, Met. Trans., 23A, 1992, pp. 1285-90.
7. J. S. Forrester, G. B. Schaffer, Met. Mater. Trans., 26A, 1995, pp. 725-730.
8. G. B. Schaffer, P.G. McCormick, Scripta Met., 23, 1989, pp. 835-838.
9. J. Kaneko, D. G. Kim, M. Sugamata, Proc. 2nd Int. Conf. on Structural Applications of Mechanical Alloying, 1993, pp. 261-268.
10. C. Chakurov, V. Rusanov, J. Koichev, J. Sol. State Chem., 71, 1987, pp. 522.
11. H. G. F. Wilsdorf, Dispersion Strengthened Aluminum Alloys, ed. Y. W. Kim and W. M. Griffith, TMS, Warrendale, PA, USA, 1988, pp. 3.
12. S. K. Das, Rev. in Particulate Materials, 1, 1993, pp. 1-40.
13. D. J. Skinner, R. L. Bye, D. Raybould, A. M. Brown, Scripta Met., 20, 1986, pp. 867.

Chapter 2 Historical Background

2.1. Mechanical Alloying

Mechanical Alloying (MA) is a room temperature powder processing technique utilizing high energy collisions of ball milling media to initiate structural changes and or chemical solid-state reactions. The repeated mechanical impacts produce intimate mixing or alloying of the powders. It is applied anywhere from the laboratory scale of a few grams of powder to commercial processes where one ton powder charges can be produced. MA has been applied in the processing of metals, intermetallics,[1-4] ceramics [5], and polymers [6] with a variety of applications in permanent magnets [7], high temperature plasma sprayed coating powders [8], immisible and amorphous alloys [4], and solid state chemical reactions[9-19].

2.1.1. Oxide Dispersion Strengthened Alloys

Mechanical Alloying was developed by Benjamin [1] as a process by which to produce oxide dispersion strengthened (ODS) alloys. The fracturing and welding of ductile materials and the fracturing of brittle materials, which occur during MA, create a fine and uniform distribution of oxide particles, which provide the strengthening in these alloys. Commercially, a range of nickel-, iron-, and aluminum based ODS alloys are produced for applications in turbine blades, gas turbine vanes and high temperature corrosion resistant plates [20].

2.1.2. Metal-Metal Alloying

Mechanical alloying is capable of creating several useful material characteristics. It leads to a very uniform mixing of the alloying materials. It leads to a very uniform particle size. MA is a high energy process that can accelerate solid state or chemical reactions. Lastly, mechanical alloying is done at room temperature so it can be used to produce metastable components which may undergo changes at higher temperatures [21]. Several simultaneous actions are taking place during the mechanical alloying process. As powder particles become trapped between the milling media, the high energy impact can weld the particles together as depicted in Fig. 1a. Also, dislocation strain hardening occurs in the particles which leads to their eventual fracture. The combination of welding and fracture leads to a kneading action which produces MA's homogeneous structures. Initially, the welding and fracture lead to the development of a lamellar structure as shown in Fig. 1b. As milling continues, the lamella thickness decreases until eventually a homogeneous mixture is produced as represented in the basic relationship shown in Fig. 1c. Another advantage of MA is the uniform particle size distribution which it produces. As the MA process proceeds, a steady state occurs between the fracture and welding of the particles. The steady state leads to particle size stabilization of the product.

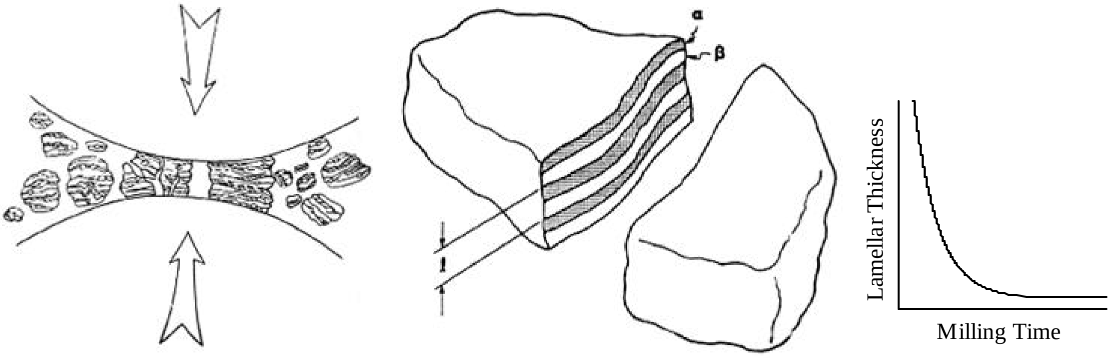

a. b. c.

Fig 1. a. Fracture and welding occur as the result of powder being trapped between milling balls [21]. b. As a result of welding and kneading, a lamellar structure develops [21]. c. As milling continues, the lamellar thickness decreases exponentially until a homogeneous mixture is produced.

Since MA is a solid state room temperature process, it allows many processes and reactions to occur that are difficult to achieve through conventional processing and synthesis techniques. An example might be production of alloys which are immisible in the solid phase. Iron and copper undergo massive segregation when cooled from a melt. When the two constituents are combined by mechanical alloying, a homogeneous distribution can be produced [22]. High differences in melting temperatures between the two elements is another instance when MA is useful. Nb_3Sn is a superconducting intermetallic which is difficult to produce by melt processes because of differences in melting temperatures [23]. MA, once again, can produce the desired homogeneity. MA also has the ability to cause amorphization. After forming an alloy of two different elements, repeated mechanical alloying, in some systems, can lead to disorder and amorphization [4].

2.1.3. The Physics of Mechanical Alloying

Mechanical alloying has always lacked clear scientific explanations of the mechanisms of the process. Several attempts have been made to model the mechanical alloying process and to explain the mechanisms which result in its unusual products. Early work by Gilman and Benjamin established estimates for the number of collisions individual particles experience based on fixed milling conditions [24]. They found for a typical SPEX mill with a 5g powder charge, there were approximately 76.8 collisions/particle/15 minutes of mill operation. Schwarz and Koch [25] analyzed temperature increases which result from the shearing of powders trapped between two colliding balls. They developed a relationship:

$$\Delta T = \frac{F}{2}\left[\frac{\Delta t}{p k_o r_p c_p}\right]^{\frac{1}{2}} \qquad (2.1)$$

$$F = s_n \bullet n_r \qquad (2.2)$$

where ΔT is the temperature increase, σ_n is the normal stress due to a head on collision, ν_r is the relative preimpact velocity of the balls, Δt is the stress state lifetime, ρ_p is the powder particle density, k_o is the thermal conductivity of the powder, and c_p is the specific heat of the powder. Schwarz estimated a collision velocity of 2 m/s and a stress state lifetime of ~2.1µs. For most milling conditions, this corresponds to a bulk powder temperature increase of less than 50°K.

Davis et.al. [26] looked at several brittle material systems in an attempt to also determine the average temperature increase and ball velocity during mechanical alloying. Using a 76mm x 57mm tool steel vial and 7.9mm diameter 440C stainless steel milling balls with a 5:1 charge ratio, estimates for maximum ball velocity were set at 18.7 m/s. At that maximum velocity, the ball would impart a high kinetic energy impact in the range of 10^{-1} J. Davis et.al. statistical calculations showed that the majority of collisions occurred with a velocity of 6 m/s and a kinetic energy dissipation of < 10^{-2} J. They also determined that the temperature increase per powder particle during milling was less than 300°K. Another critical aspect of their work involved video analysis of the MA process using a transparent milling vial. By studying collisions during milling, they determined a quantitative number of ball to ball collisions that occurred during a set milling time and placed estimates on the energy associated with each impact. Only 0.4 percent of all recorded collisions occurred as high energy (>10^{-2} J) head-on or near head-on (±10°) collisions.

Maurice and Courtney have done extensive work on the physics and mechanics of mechanical alloying [21,27-31]. In their first attempt to explain the physics of MA, they also studied the preimpact ball velocity and temperature rises which could occur during MA. In addition, they looked at the affects of the volume of powder involved in impacts, milling time, charge ratio, and different MA milling equipment. In their Hertzian approach, they viewed impacts during MA as miniature powder forging events. The preimpact velocity of the balls was estimated by assuming that a SPEX mill operated as a linear harmonic device and using the vial dimensions and cyclic frequency of the mill, a velocity of 3.9 m/s was determined. Temperature increases during milling were calculated based on the assumption that heat generated during MA impacts was similar to heat created during other metal forging events. The resulting equation for temperature increase per collision was:

$$\Delta T = \frac{1}{C_p}\left[s_o e_{\max} + \left[K e_{\max}^{n+1}/(n+1)\right]\right] \tag{2.3}$$

where ΔT is the temperature increase, C_p is the specific heat of the powder, e_{max} is the maximum powder strain per collision, n is the strain hardening coefficient of the powder, and s_o and K are constants. Using this equation, Maurice and Courtney calculated temperature increases as high as 630°K for niobium powder milled using a SPEX mill at a 10:1charge ratio with 0.64 cm balls. For aluminum, however, the temperature increase using the same milling conditions was estimated to only be 8°K.

2.1.4. Mechanochemical Reactions

A significant amount of work has been done on the effect of MA on chemical reactions. Of particular interest has been the research into mechanical alloying and displacement reactions. Schaffer and McCormick have discovered that CuO could be reduced by Ca using MA as the initiation mechanism. In addition, they discovered that β'-brass could be formed by using Ca to reduce a mixture of CuO and ZnO [9,10]. Since those discoveries, numerous other investigations have been performed using MA in conjunction with displacement reactions. CuO has been reduced by Al, Mg, Ti, Mn, Fe, or Ni [11-13]. Ti was used to reduce ZnO [14]. A nice review of this work was done by McCormick [15] Of particular interest to this work, Al has been used with MA to reduce Fe_2O_3 [16-18] and SiO_2 [19].

Schaffer and McCormick used the work with displacement reactions to begin to investigate the kinetics of mechanical alloying [12-13]. They tried to look at how factors such as defect structures and densities, local temperatures, high reaction interface areas, and product morphology influenced diffusion rates. Their work with the CuO + Fe displacement reaction showed that there was a decrease in the heat-treatment-induced reaction ignition temperature with increasing MA milling time. The decrease of the reaction ignition temperature was further enhanced by increasing the charge ratio. For reactions occurring during milling, they showed an inverse relationship between charge ratio and reaction ignition time. They were unable, however, to determine a specific energy input from mechanical alloying [12]. Schaffer and McCormick's explanation for the changes in reaction ignition were based on the premise that mechanical alloying changes the dominant rate-controlling step for displacement reactions from bulk lattice diffusion to diffusion down short-circuit pathways. Their evidence was a significant decrease in the apparent activation energy calculated from differential thermal analysis results for reactions following mechanical alloying [13].

2.2 Displacement Reactions

A displacement reaction is a chemical reaction in which a metal oxide is reduced by a reactive metal to form the metal and the reactive metal oxide. Some displacement reactions are also self-propagating, i.e., when reagents are ignited, they spontaneously react to form products. These reactions are highly exothermic and, hence, supply the energy necessary to drive the reaction to completion. The term “thermite” reaction has been applied to such reactions. Typical thermite reactions are exemplified by the reduction of Fe_2O_3 or SiO_2 by aluminum as described by equations 2.1 and 2.2.

$$2Al + Fe_2O_3 \rightarrow 2Fe + Al_2O_3 \tag{1.1}$$

$$4Al + 3SiO_2 \rightarrow 3Si + 2Al_2O_3 \tag{1.2}$$

Thermite reactions have historically been used in many engineering applications. Goldschmidt and co-workers, who coined the term thermite, were using the reactions as a reducing agent to form chromium, manganese and other metals as early as 1898 [32-33]. The relative energy involved in a thermite reaction can be seen in Fig. 2 where a mixture of Al and Fe_2O_3 are mixed and the reaction is initiated [34].

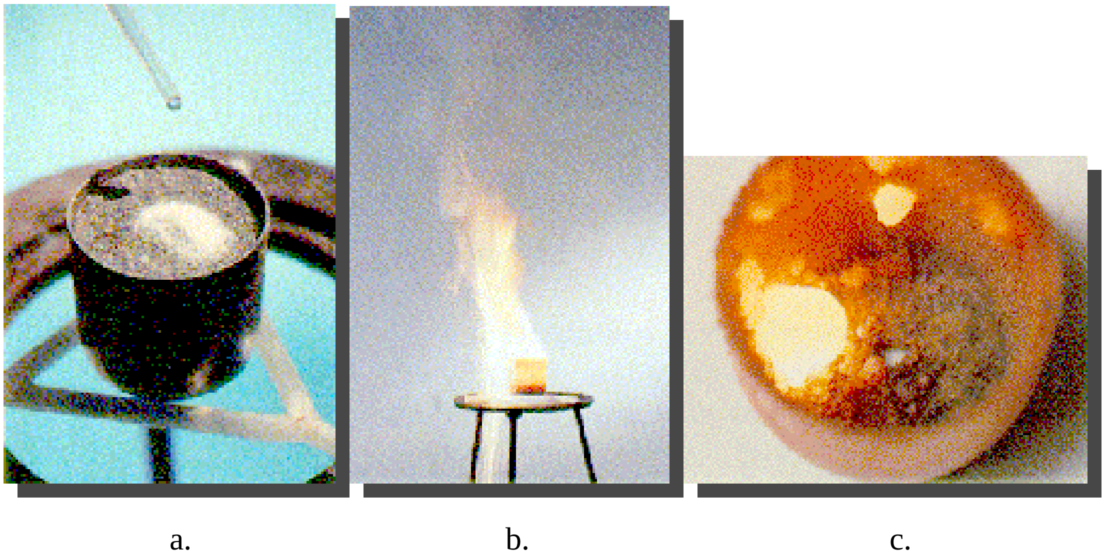
a. b. c.

Fig. 2. Basic thermite process. a. Mixture of Al and Fe_2O_3. b. During reaction. c. After completion of reaction [34].

Because the thermite process is a relatively low cost option in terms of equipment and materials, it has become popular in applications such as rail welding [35] and in the synthesis of new materials [36].

Self-propagating high-temperature synthesis (SHS) reactions are close cousins of displacement reactions. The SHS process was originally developed in Russia in the 1960’s and was recently introduced in the U. S. by Lockheed Martin Corp. as the XD^{TM} (eXothermic Dispersion) process. In XD, a reactive metal is mixed with various other precursor materials. Then, the highly exothermic reaction is initiated. The resulting product is a dispersion of fine particles in a matrix. An example of the process is the mixing and reaction of Ti, Al and B to form a TiB_2 - reinforced TiAl composite [37].

2.3. Strengthening Mechanisms in Aluminum

There are 5 principle mechanisms which can contribute to increased strength in aluminum and other metallic material systems. These mechanisms can be active as individual components or work together in combination to increase strength. With the exception of composite strengthening which is primarily a mechanical load transfer, the key room temperature principle is to inhibit dislocation glide. At elevated temperatures, where other deformation mechanisms may be active, inhibiting the primary deformation mechanism is the key. Since the focus of the work was to provide high temperature strength, alloy selection and processing focused on activating mechanisms which were most effective at strengthening at high temperatures.

2.3.1. Dislocation Work Hardening

The most basic strengthening mechanism in any metallic system is dislocation work hardening. As a metal is deformed, massive quantities of dislocations are produced. With so many dislocations moving throughout the metal, it is inevitable that they will intersect. These interactions limit a dislocations mobility and result in a strengthening effect.

The flow stress of a pure metal is often estimated using the Taylor Relation [38] shown in Equation 2.3.

$$s = aGbr^{1/2} \tag{2.4}$$

where s is the flow stress, a is a constant which is ~ 0.2 for fcc metals, G is the shear modulus, b is the burgers vector and r is the dislocation density. For annealed aluminum, a minimum flow stress of 4.72 MPa is estimated using values of $r = 1 \times 10^{13}$ m^{-2} , $b = 2.86 \times 10^{-10}$m, G = 26.1 GPa and $a = 0.2$. For heavily cold worked aluminum, a maximum flow-stress of 106 MPa can be estimated using a dislocation density of $r = 5 \times 10^{15}$ m^{-2}. Work hardening can therefore be considered a significant contributor to increased strength in aluminum. However, the maximum estimated flow strength values are below many typical engineering requirements. Other strengthening mechanisms are necessary in conjunction with work hardening to improve room temperature strength values.

Beyond the inability to achieve desired strength levels alone, cold working is an inappropriate approach for achieving any portion of strengthening in high temperature aluminum alloys. Considering that high temperature alloys are used at or above 1/2 the homologous melting temperature, the unstable nature of cold work becomes problematic. At those elevated temperatures, the processes of recovery and recrystallization will remove the effects of cold work. The stored energy of cold work is the primary driving force for both of these processes. Recovery can basically be defined as the reduction of the dislocation line energy stored during deformation. The reduction occurs by the polygonization into subgrains and annihilation of dislocations. Recrystallization is the nucleation and growth of new grains but can also include the coalescence of polygonized cells. Both recovery and recrystallization lead to reductions in strength. It is therefore necessary to avoid cold work in high temperature alloys.

2.3.2. Solid Solution Strengthening

There are two basic types of solid solutions, substitutional and interstitial. Both create localized stress fields which are caused by differences in the atomic size between the solute and solvent atoms. When just considering moving dislocations, it is the stress fields and contributions from moduli differences between solute and solvent atoms which inhibit dislocation motion and cause strengthening. Mott and Nabarro [39] developed a relationship for strengthening which incorporated the amount of the internal stress fields as a function of the change in the lattice parameter of the solid solution caused by the atomic concentration of solute. Fleisher [40] later added to the relationship by including a contribution due to the shear modulus of the solute atoms. Equation 2.4 shows both of these contributions:

$$\Delta t = \frac{1}{a}\left(\frac{da}{dc}\right) + \frac{1}{G}\left(\frac{dG}{dc}\right) \tag{2.5}$$

where *a* is the lattice parameter of the solid solution, *da/dc* is the change in the lattice parameter with respect to the concentration of solute, *G* is the shear modulus of the solute atom, and *dG/dc* is the change in the shear modulus of the solution with respect to the solute concentration. For both contributions, the solid solubility (solute concentration) is critical. In the current work, the solubility of iron, silicon, and oxygen in aluminum, the major elements present, is extremely limited (<0.1 wt%). As a result, solid solution strengthening will most likely be limited.

Substitutional solid solution strengthening in aluminum is generally low. This is because of its fcc crystal structure and the symmetrical nature of the corresponding substitutional atom sites. In fcc crystals, the stress field created by a substitutional atom is symmetrical. Symmetrical stress fields will only interact with edge dislocations and thus limit the possible strengthening. When the stress field for solute atoms is non-symmetrical, as for carbon in iron, both screw and edge dislocations will interact. This leads to a much stronger strengthening effect [41].

2.3.3. Boundary Strengthening

Most metals show a strong relationship between grain size and strength. The smaller the grain size, the higher the associated flow stress. An empirical relationship between flow stress and grain size, simultaneously developed by Hall [42] and Petch [43], is shown in Equation 2.5.

$$s = s_o + kd^{-1/2} \tag{2.6}$$

In the Hall-Petch equation, as Equation 2.5 is commonly known, s is the flow stress, s_o and k are constants taken from linear fitting of the experimental data and d is the average grain diameter.

Hall and Petch rationalized that in order for deformation to occur via dislocation motion, dislocations had to propagate from a deformed grain to an undeformed grain with grain boundaries acting as obstacles to this motion. Dislocations would pile-up at a grain boundary leading to a stress concentration at the boundary. This pile-up would lead to the development of a stress concentration in an adjacent grain with a magnitude which corresponds to the number of dislocations in the pile-up. Therefore, fine-grained materials would have a smaller number of dislocations piled-up at the boundaries leading to reduced stress concentrations in adjacent grains and the ability to sustain a greater applied stress.

When compared to other metals, the grain size strengthening effect in aluminum is very small. The Hall-Petch constants for pure aluminum as well as copper, titanium and Armco iron are shown in Table 1. The k term is essentially a measure of the extent to which dislocations are piled up at the grain boundary. The s_o constant is a measure of the stress required to push dislocations against the resistance of impurities, particles and the Peierls force. One explanation for the small Hall-Petch constants is that cross slip is easier in fcc materials such as aluminum and copper, thus allowing dislocations to easily bypass impurity particles and reduce piling up at grain boundaries [44]. Utilizing the Table 1 values for aluminum in Eq. 2.5 with an average grain diameter of 100 μm, the flow stress would be 22.5 MPa. For an average grain diameter of 1 μm, the flow stress would be 83.9 MPa. The key aspects for utilizing the boundary strengthening effects with high temperature alloys is to first, achieve a fine grain structure and second, prevent its growth. This is one area where the utilization of a mechanical alloying method in combination with dispersion strengthening will become advantageous.

Table 1. Hall-Petch constants for several common metals

Metal	σ_o (MPa)	k ($MPa \cdot mm^{0.5}$)
Aluminum	15.7	2.16
Titanium	78.5	12.75
Armco Iron	74.5	18.44
Copper	25.5	3.53

2.3.4 Particle Strengthening

There are two different particle - dislocation interactions which lead to strengthening; particle shearing and particle looping. Particle shearing occurs in the case of very small (soft) particles which maintain a coherent interface between themselves and the surrounding matrix material. Dislocations will glide through the particle as shown in Figure 3 [45]. In general, the strengthening provided is dependent on the size, shape, and volume fraction of particles. However, there are numerous specific mechanisms which may or may not be present with shearable particles including chemical strengthening, modulus mismatch, lattice mismatch, order strengthening or stacking fault energy mismatch. Each mechanism and its corresponding simplified explanation are shown in Table 2.

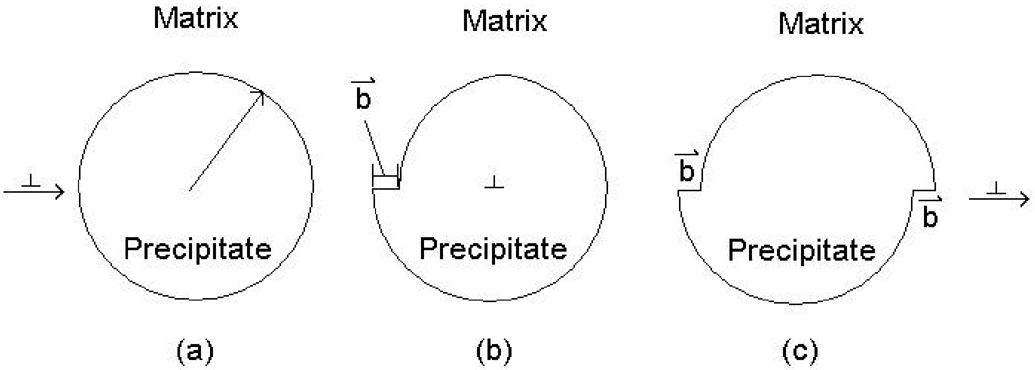

Fig. 3. Propagation of an edge dislocation through a shearable precipitate particle. a. dislocation approaches particle. b. Dislocation enters particle. c. Dislocation has passed through particle and continues to glide [45].

Table 2. Strengthening mechanisms for shearable particles

Mechanism	Explanation
Chemical Strengthening	Strengthening results from the energy required to create additional surface area in the sheared particle.
Order Strengthening	Strengthening results from the energy required to create an anti-phase boundary in an ordered particle.
Lattice Mismatch	Stress fields caused by the coherent particle-matrix interfaces result in elastic dislocation interactions.
Modulus Mismatch	Shear modulus differences between particles and the matrix result in elastic dislocation interactions.
Stacking Fault Energy Mismatch	Stacking fault energy differences between particles and the matrix result in elastic dislocation interactions

Nembach [46] developed a basic relationship for shearable particle strengthening which for many systems is of the form

$$t_p = CD^{3/2}(rf/2S)^{1/2} \tag{2.7}$$

where C is a constant, D is a function which specifies the strengthening mechanism which is active in the material system, r is the average particle radius, f is the particle volume fraction, and S is the dislocation line tension. For a single type of particle, numerous mechanisms may be present in a single system and the strengthening would be additive.

As a coherent shearable particle grows in size, the strains associated with lattice parameter mismatch become great enough to create accommodation dislocations along the particle/matrix interface. This is known as a semi-coherent interface. Eventually, the particles grow to sizes where there is little coherency between the matrix and particles and the resulting interface is commonly referred to as incoherent, although there still remains some coherency between the two interfaces .

Particle looping, in most cases, occurs with incoherent particles. It can also occur in coherent particles which are non-shearable (hard) because the stress required to shear the particle is greater than the stress to loop it. As a dislocation glides through the matrix, it encounters the incoherent interface. Since it cannot continue to pass through the particle, the dislocation begins to bend around the particle. Eventually the dislocation bends to the point where a loop is left behind surrounding the particle and the dislocation can continue to glide. Subsequent dislocations which interact with this same particle must not only bypass the particle by looping, they must also accommodate for the effects of the dislocation loop which is already present. The steps of the looping mechanism are shown in Fig. 4 [47]

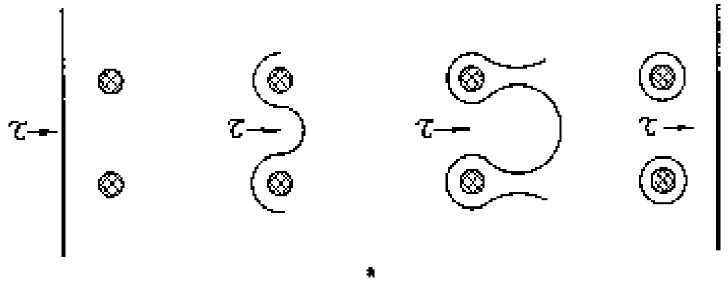

Fig. 4. Orowan looping of non-shearable particles [47]

The looping mechanism was first described by Orowan [48] who estimated the strength contribution from such a mechanism to be related to the shear modulus, burgers vector, and the interparticle spacing.

Numerous modifications have been made to Orowan's original relationship and one currently accepted version is known as the Ashby - Orowan relationship [49]:

$$\Delta t = \frac{0.81Gb}{2p\left(1-u\right)^{1/2}} \bullet \frac{\ln\left(2r_p / r_o\right)}{l_{eff}} \tag{2.8}$$

$$l_{eff} = 1.25r_p\left(\frac{2p}{3f}\right)^{1/2} - 2\sqrt{2/3} \bullet r_p \tag{2.9}$$

where G is the shear modulus, b is the burgers vector, v is the Poisson's ratio, r_p is the particle radius, r_o is the dislocation core radius, λ_{eff} is the calculated effective particle spacing , and f is the volume fraction. Therefore, as the number of loops around a particle increase, the particle spacing is reduced and strengthening increased.

Kelly has made a modification to Equation 2.7 which corrects for non-spherical rod shaped particles which is known as the Ashby-Orowan-Kelley equation [50]:

$$\Delta t = \left(\frac{0.81Gb}{2p\left(1-u\right)^{1/2}}\right) \bullet \left(\frac{1+(l / l_{eff})}{l_{eff}}\right) \bullet \ln\left(t / r_o\right) \tag{2.10}$$

$$l_{eff} = \left(\frac{l \cdot t}{f}\right)^{1/2} \tag{2.11}$$

where G is the shear modulus, b is the burgers vector, v is the Poisson's ratio, l is the particle length, t is the particle thickness, r_o is the dislocation core radius, l_{eff} is the particle spacing , and f is the volume fraction.

For particles to have a significant contribution to strengthening by dislocation looping mechanisms, their size should be less than 1μm. As particle size increases (1 μm < p.s. < 10 μm) dislocation interactions decrease and strengthening can occur by grain size refinement. The particles can act to pin grain boundaries resulting in a small average grain size.

2.3.4.1. Precipitation Strengthened Alloys

A large portion of the aluminum alloys used in engineering applications fall into the category of precipitation strengthened alloys. Most are produced by heat treating and quenching to produce a supersaturated solid solution. Then, they are aged to create the precipitates. As the precipitates form, they maintain a coherent interface with the matrix. In most cases, the coherent precipitates will behave as shearable particles. As the precipitates grow, coherency is lost and strengthening occurs by particle looping. One requirement for precipitation strengthening is the ability to create a supersaturated solid solution of high enough concentration that a significant volume fraction of precipitates can be formed during aging. In the cases of the Fe and Si in Al, there is very little solubility even at high temperatures, based on binary phase diagrams. As a result, the ability to precipitation strengthen will be limited.

Another negative attribute of precipitation strengthening is the thermal instability of precipitates. In high temperature applications, most precipitates will rapidly coarsen and lose their strengthening potential. As a result, precipitation strengthening was historically avoided for high temperature applications involving aluminum. Recently, however, extensive research has been performed on precipitation strengthened aluminum alloys which have been able to avoid the problems of thermal stability and limited solubility. These alloys have been based in the Al-Fe system [51-56].

Al-Fe intermetallic compounds, such as $Al_{13}Fe_4$ and Al_6Fe, have a relatively low permeability (1.12×10^{-15} at.% cm^2/s) compared to compounds commonly used for precipitation strengthening such as Al_2Cu (1.60×10^{-10} at% cm^2/s). A low permeability (the product of maximum solid solubility and diffusivity at the maximum use temperature) is necessary to resist particle coarsening at elevated temperatures. However, with the low permeability comes the problem of low solid solubility and the inability of solutionizing and aging to create precipitates. Researchers have successfully produced Al-Fe based precipitates by using rapid solidification techniques. Rapid solidification, like mechanical alloying, can extend solubility limits. At Alcoa, an Al-Fe-Ce alloy, produced using gas atomized powder and powder metallurgy (P/M) techniques, is capable of extended service temperatures to ~300°C [51]. An alloy formerly produced by Allied Signal (alloy 8009) and patented by the University of Virginia [52] was produced by planar flow casting of ribbon, communition into powder, and densification by P/M techniques [53]. In alloy 8009, very fine $Al_{12}(Fe,V)_3Si$ precipitates (20-50 nm) provide improved elevated strength and thermal stability to temperatures in excess of 425°C [54-56].

2.3.4.2. Dispersion Strengthened Alloys

Incoherent particles can also be produced in the matrix by methods other than particle coarsening. Particles can be mixed into the matrix using powder metallurgy techniques, or produced using in-situ chemical reactions. In these cases, the particles will be termed dispersoids, and will be considered to be inert, thermally stable within the matrix, and non-shearable. Dispersion strengthening has been around almost as long as metallurgy itself. Copper awls which are approximately 9000 years old were produced by a repeated forging, hammering and welding process which resulted in a layered structure of copper reinforced by oxide inclusions [57]. More modern examples of dispersion strengthening can be traced to patents by Schmid in 1924 for the sintering of a mixture of Al and Al_2O_3 particles [58]. This led, in the 1940's, to commercial manufacture of SAP (sintered aluminum product) alloys produced by sintering powders which were ball milled in oxidizing atmospheres [59]. Theoretical treatments did not begin to appear until the 1950's and 1960's [49,60-62]. In all cases, the challenge of dispersion strengthening is to produce a fine, uniform distribution of particles in the matrix. One technique which has been successfully utilized is mechanical alloying. Commercially, a range of nickel-, iron-, and aluminum-based oxide dispersion strengthened (ODS) alloys are produced for applications in turbine blades, gas turbine vanes and high temperature corrosion resistant plates. More recent techniques have utilized mechanical alloying in combination with chemical reactions to create Al alloys containing dispersoids of Al_2O_3 and Al_4C_3. These DISPAL^{TM} alloys show promise for achieving good high temperature properties [63].

2.3.5. Composite Strengthening

Composite materials have a long and varied history. Nature provides us with many examples of composites. Wood can be considered a composite of cellulose fibers reinforcing a lignin matrix. Probably the first man-made composites were building bricks made of mud and straw [64]. The beginnings of modern composites can be traced to the extensive research on dispersion strengthened alloys. In these alloys, small precipitates or non-metallic inclusions (< 1 μm) inhibit dislocation motion and lead to strengthening of the alloy. These materials can be classified as matrix strengthening alloys but in general are not considered in composite strengthening models [57]. Although some contributions to strength can occur with spherical particles, in general as the reinforcement aspect ratio (the reinforcement length divided by the diameter) deviates from unity, a significant amount of load transfer from the matrix to the reinforcement can occur. It is this load transfer concept, occurring during elastic and plastic deformation, which generally separates composite materials from dispersion strengthened alloys.

In the 1960's, interest in fiber reinforced metal matrix composites grew. Research efforts from this period resulted in the development of boron fiber reinforced aluminum and directionally solidified eutectic in situ composites among others. In the 1970's and 1980's, fiber composite research shifted towards higher temperature materials. As a result, a variety of titanium and nickel alloy matrix materials were produced [57].

Most recently, a resurgence in particulate and whisker reinforced MMC's has occurred. This can be explained in part by the shortcomings of fiber reinforced MMC's. Mainly, particulate composites are cheaper to produce, they are compatible with existing metallurgy equipment and they are easier to join together. Examples of these developments include aluminum reinforced with SiC and Alumina whiskers [57]. The developments in composite materials have occurred very rapidly with the majority of the work being done only in the last 30 years. By combining technologies from all areas of materials science, composites should continue to enjoy the same kind of future growth.

Strengthening in metal matrix composites is predominantly mechanical in nature. High stiffness - high strength fibers are added to a ductile matrix to improve the composite modulus and strength. For short fiber or discontinuous composites, the matrix plays a much more important role in the mechanical properties. There are numerous models for estimating composite strengthening. Two of the more popular ones used with discontinuous composites are the shear lag model and the Eshelby model. The shear lag model was developed by Cox [65] with derivations for both stiffness [66] and yield strength [67]. In the model, load transfer occurs between a fiber and the matrix by shear stresses acting at the matrix-fiber interface. It is successful at estimating properties for continuously reinforced materials but tends to be less accurate with low aspect ratio reinforcements. In general, the model is good for crude estimates of stiffness for composites, however due to its simplified approach, more rigorous models are required where multiaxial stresses are incorporated.

Beginning in the 1950's, J.D. Eshelby developed a model to characterize the stresses in an ellipsoidal inclusion [68]. The model is based on the assumption that an ellipsoidal inclusion with uniform nonelastic strain is embedded in an infinite elastic body. Based on this eloquent work, Mori and Tanaka were able to modify the basic model to include multiple inclusions and their interactions[69]. Eshelby type models give much more accurate estimates of composite stiffness compared to the shear lag model.

Both shear lag and Eshelby models are strictly mechanical and do not take into account any physical changes which the reinforcements may induce in the matrix. Arsenault [70] has worked extensively on incorporating strengthening effects from residual stresses caused by differences in the thermal coefficients of expansion of the particles and the matrix. The residual stresses in the matrix lead to increases in the dislocation density. A commonly used relationship for the increase in strength is shown in Eq. 2.12:

$$\Delta\sigma_{CTE} = \alpha' \, G \, (2f\varepsilon_{\Delta CTE}/1-f)^{1/2} \, R^{1/3} \, (1+2/R)^{1/2} \, (1/V)^{1/6} \qquad (2.12)$$

$$\varepsilon_{\Delta CTE} = \Delta CTE \, \Delta T/2 \qquad (2.13)$$

where α' is a constant, G is the shear modulus, f is the volume fraction, R is the aspect ratio, V is the particle volume, ΔT is the temperature change during processing, and ΔCTE is the difference of the thermal coefficient of expansion between the matrix and reinforcement.

2.3.6. Strengthening at Elevated Temperatures

With all of these strengthening mechanisms available, it seems that there should not be a problem in producing a high-strength high-temperature aluminum alloy. The problem is, however, that most of the strengthening mechanisms previously discussed rely on dislocation glide being the means of deformation. At elevated temperatures, other deformation mechanisms can be active including dislocation creep, Coble creep, Herring-Nabarro creep, and grain boundary sliding. Dislocation creep, also known as power law creep, occurs as the result of dislocation climb aided by diffusion of vacancies. High temperature dislocation creep occurs as the result of diffusion of vacancies through the lattice. Low temperature dislocation creep is believed to occur by diffusion of the vacancies along dislocation cores. Coble and Herring-Nabarro creep, also known as diffusional flow, occur via mass transport. For Herring-Nabarro, transport is through the lattice. While for Coble creep, transport occurs along grain boundaries. The key to high-temperature strengthening is determining which deformation mechanism will dominate. A convenient method for this is deformation mechanism maps. They incorporate all the relationships for creep and combine them on a chart of stress and temperature. A deformation mechanism map for pure aluminum with a grain size of 10 μm is shown in Fig. 5 [71].

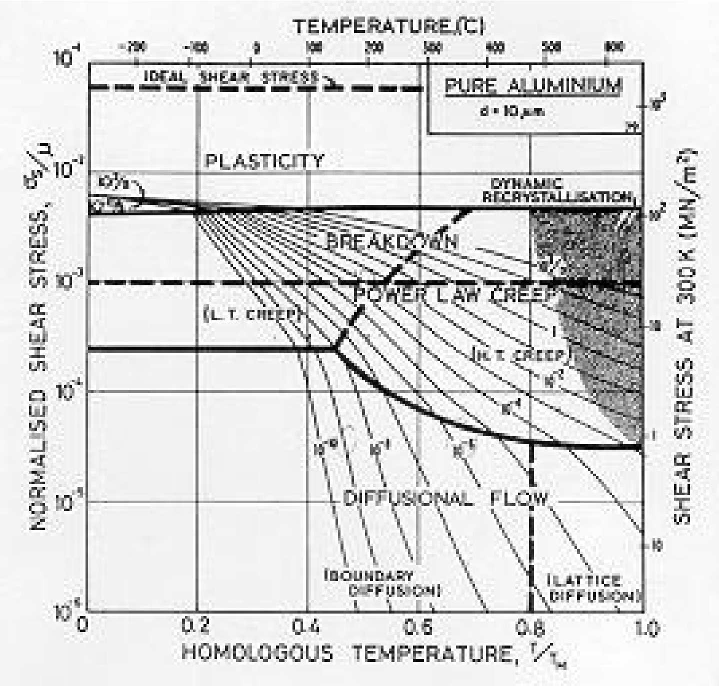

Fig. 5. Deformation mechanism map for pure aluminum with a 10 μm grain size [71].

In powder metallurgy alloys, very fine grain and subgrain structures are produced. As a result, diffusion distances are small and an interface controlled deformation mechanism may dominate. If diffusional creep occurs by the generation or absorption of vacancies by dislocations in the interface, then the interface dislocations should be mobile. If, however, the motion of the boundary dislocations is impeded by fine, closely spaced particles, the deformation by diffusional creep would be slowed. Therefore, strengthening methods which block dislocation motion may be effective at elevated temperatures also. Some evidence of this can be seen for some oxide dispersion strengthened alloys [72] as well as the newer rapidly solidified Al-Fe based alloys discussed earlier [51].

2.4 Densification of Aluminum Powders

There are numerous conventional and novel techniques for the densification of metal powders. The conventional methods require pressing of powder followed by high temperature sintering. Pressing is accomplished by uniaxial die compaction or cold isostatic pressing. Newer methods of densification include hot isostatic pressing, powder extrusion and explosive compaction. The two techniques used in this work will briefly be discussed.

2.4.1. Uniaxial Die Compaction

Uniaxial compaction using hard tooling in a hydraulic or mechanical press is the most common method of densifying metal powders. This type of compaction allows for pressing of parts to very close dimensional tolerances. However, density gradients can develop in the pressed parts due to die wall friction. Density gradients will lead to variation in shrinkage and distortion of the compact during sintering. In general, density gradients can be reduced if a low profile compact with a small height to diameter ratio is pressed. Uniaxial die compaction is, therefore, not practical for the production of rod shaped parts [73].

Uniaxial compaction is not capable of producing fully dense parts, and a subsequent sintering operation is required. Sintering is the welding of particles together at high temperatures. Sintering is normally accomplished at temperatures well below the melting point. It occurs by mass transport to regions of contact between particles. The driving force is the elimination of the high surface energy of powder materials [74-75]. It is through the process of pressing and sintering that the majority of powder metal products are manufactured.

2.4.2. Powder Extrusion

Powder extrusion is a useful method for the production of full density rod shaped parts. Powders are degassed and vacuum sealed in a suitable metal can. The can is then heated and forced through a small die opening. A schematic drawing of powder extrusion is shown in Fig. 6. The technique is useful for densification of materials such as mechanically alloyed or rapidly solidified powders where other techniques such as high temperature sintering may alter the desired structure.

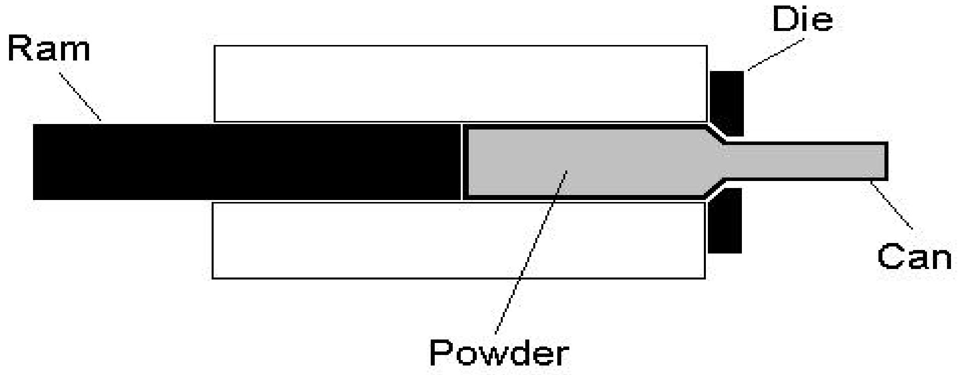

Fig. 6. Schematic of process for densification by extrusion of canned powder metal.

References

1. J. Benjamin, Met. Trans., 5, 1974, pp. 1929-34.
2. A. O. Aning, Z. Wang, T. H. Courtney, Acta Metall. Mater., 41, 1993, pp. 165-174.
3. M. Oehring, Z. H. Yan, T. Klassen, R. Borman, Physica Status Solidi A, 131, 1992, pp. 671-89.
4. A. W. Weeber and H. Bakker, Physica B, 153, 1988, pp. 93-135.
5. A. O. Aning, C. Hong, and S. B. Desu, Mater. Sci. Forum, Mechanically Alloyed and Nanocrystalline Materials, Ed. R. Yavrai, 179-181, 1995, pp. 207-214.
6. J. Pan, W. J. D. Shaw, Proc. 24th Int. SAMPE Tech. Conf., 24, 1992, T762.
7. A. Y. Yermakov, Mat. Sci. Forum, 88-90, 1992, p. 577.
8. J. R. Rairden, E. M. Habesch, Thin Solid Films, 83, 1981, p. 353.
9. G. B. Schaffer, P.G. McCormick, Scripta Met., 23, 1989, pp. 835-838.
10. G. B. Schaffer, P.G. McCormick, Appl. Phys. Lett., 55, 1, 1989, pp. 45-46.
11. G. B. Schaffer, P.G. McCormick, Met. Trans., 21A, 1990, pp. 2789-94.
12. G. B. Schaffer, P.G. McCormick, Met. Trans., 23A, 1992, pp. 1285-90.
13. J. S. Forrester, G. B. Schaffer, Met. Mater. Trans., 26A, 1995, pp. 725-730.
14. G. B. Schaffer, P.G. McCormick, Met. Trans., 22A, 1991, pp. 3019-3024.
15. P. G. McCormick, Materials Transactions, JIM, 36, 2, 1995, pp. 161-169.
16. J. Kaneko, D. G. Kim, M. Sugamata, Proc. 2nd Int. Conf. on Structural Applications of Mechanical Alloying, 1993, pp. 261-268.
17. P. Matteazzi, G. LeCaer, Hyperfine Interactions, 91, 1991, pp. 177-180.
18. D. Basset, P. Matteazzi, F. Miani, G. LeCaer, Hyperfine Interactions, 94, 1994, pp. 2235-2238
19. G. T. Hida, I. J. Lin, Combustion and Plasma Synthesis of High Temperature Materials, Ed. Z. A. Munir and J. B. Holt, VCH Pub., New York, 1990, pp. 246-261.
20. R. Sundaresan, F. H. Froes, J. of Metals, 39, 1987, p. 22.
21. D. R. Maurice,T. H. Courtney, Metall. Trans., 21A, 2, 1990, pp. 289-303.

22. J. Benjamin, Mat. Sci. Forum, 88-90, 1992, pp. 1-17.
23. R. L. White, W. D. Nix, New Devel. & Appl. in Composites, D. Kuhlmann-Wilsdorf and W. C. Harrigan, Eds., TMS, AIME, Warrendale, PA, 1979, p. 78.
24. P. S. Gilman, J. S. Benjamin, Ann. Rev. Mater. Sci., R. A. Huggins, R. H. Bube, and D. A. Vermilyea, eds., Annual Reviews Inc., Palo Alto, CA, 1983, vol. 13, p. 279.
25. R. B. Schwarz, C. C. Koch, Appl. Phys. Lett., vol. 49, 1986, p. 146.
26. R. M. Davis, B. McDermott, C. C. Koch, Metall. Trans., vol 19A, 1988, pp. 2867-2874.
27. D. R. Maurice,T. H. Courtney, Metall. Trans., vol. 25A, 1994, pp. 147-158.
28. D. R. Maurice,T. H. Courtney, Metall. Trans., vol. 26A, 1995, pp. 2431-2435.
29. D. R. Maurice,T. H. Courtney, Metall. Trans., vol. 26A, 1995, pp. 2437-2444.
30. D. R. Maurice,T. H. Courtney, Metall. Trans., vol. 27A, 1996, pp. 1973-1979.
31. D. R. Maurice,T. H. Courtney, Metall. Trans., vol. 27A, 1996, pp. 1981-1986.
32. H. Goldschmidt and C. Vautin, J. Soc. Chem. Ind., 19, 543, (1898).
33. H. Goldschmidt and O. Weil, US Pat. 895 628, (1908).
34. R. J. Gillespie, Atoms, Molecules and Reactions, Prentice-Hall, Englewood Cliffs, NJ, 1994.
35. A. J. Key, Aust. Weld. J.,3, 15, (1985).
36. Z. Munir, Ceramic Bul., 67, 342-349, (1988)
37. R. K. Everett, R. J. Arsenault, Metal Matrix Composites: Processing and Interfaces, Academic Press, Boston, 1991, pp. 127.
38. G. I. Taylor, Proc. Roy. Soc., A145, 1934, pp. 388.
39. N. F. Mott, F. R. N. Nabarro, Bristol Conf. on the Strength of Solids, Physical Society, London, 1948, p. 1.
40. R. L. Fleischer, Acta Met, 11, 1963, p. 203.
41. R. W. Hertzberger, Deformation and Fracture Mechanics of Engineering Materials, 3rd ed., Wiley, New York, 1989, p. 121.
42. E. O. Hall, Pro. Phys. Soc. London, B64, 1951, p. 747.
43. N. J. Petch, J. Iron and Steel Inst., 174, 1953, p. 25.
44. A. W. Thompson, M. I. Baskes, Philosophical Magazine, vol. 28, 1973, pp. 301-308.
45. T. H. Courtney, Mechanical Behavior of Materials, McGraw-Hill, New York, 1990, p. 187.
46. E. Nembach, Particle Strengthening of Metals and Alloys, John Wiley, New York, 1997, p. 228.
47. M. A. Meyers, K. K. Chawla, Mechanical Metallurgy, Prentice-Hall, Englewood Cliffs, NJ, 1984, p. 410.
48. E. Orowan, Symp. on Internal Stresses in Metals and Alloys, Inst. Metals, London, 1948.
49. M. F. Ashby, Proc. 2nd Bolton Landing on Oxide Dispersion Strengthening, Ed. G. S. Ansell, T. D. Cooper, F. V. Lenel, Gordon Breach, New York, 1968, pp. 143-209.
50. P. M. Kelley, Int. Metall. Rev., 18, 1973, pp. 31-36.
51. S. K. Das, Rev. in Particulate Materials, 1, 1993, pp. 1-40.
52. G. J. Shiflet, S. Poon, Y, He, U. S. Patent 4964927, 1989.
53. D. J. Skinner, R. L. Bye, D. Raybould, A. M. Brown, Scripta Met., 20, 1986, p. 867.
54. D. J. Skinner, Dispersion Strengthened Aluminum Alloys, Ed. Y. W. Kim, W. M. Griffith, TMS, Warrendale, PA, 1988, pp. 181-197.
55. S. K. Das, L. A. Davis, Mat. Sci. and Eng., 98, 1988, pp. 1-12.
56. V. R. V. Ramanan, D. J. Skinner, M. S. Zedalis, Mat. Sci. and Eng. A134, 1991, pp. 912-916.

57. T. W. Clyne, P. J. Withers, Introduction to Metal Matrix Composites, Cambridge University Press, Cambridge, 1993, p. 3.
58. E. Schmid, German Patents, Nos. 425451, 425452, 427370, 1924.
59. J. H. Weber, Mechanical Properties of Metallic Composites, Ed. S. Ochiai, Marcel Dekker, 1993, pp. 269-291.
60. R. B. Nicholson, Strengthening Methods in Crystals, Applied Sci. Pub., Essex, 1971, pp. 535-613.
61. L. M. Brown, R. K. Ham, Strengthening Methods in Crystals, Applied Sci. Pub., Essex, 1971, pp. 12-135.
62. N. Hansen, Dispersion Strengthened Aluminum Products-Manufacture, Structure, and Mechanical Properties, Riso National Lab, Denmark, 1971.
63. V. Arnhold, K. Hummert, Dispersion Strengthened Aluminum Alloys, Ed., Y. W. Kim and W. M. Griffith, TMS, Warrendale, PA, 1988, pp. 483-500.
64. K. K. Chawla, Composite Materials: Science and Engineering, Springer-Verlag, Berlin, 1987.
65. H. L. Cox Jr., J. Appl. Phys., 3, 1952, p. 72.
66. A. Kelly, Strong Solids, Clarendon Press, Oxford, 1966.
67. V. C. Nardone, K. M. Prewo, Scripta Metall., 20, 1986, pp. 43-48.
68. J. D. Eshelby, Proc. Roy. Soc. Lond., A241, 1957, p. 376.
69. T. Mori, K. Tanaka, Acta Metall., 21, 1973, p. 571.
70. R. J. Arsenault, Composite Structures 4, vol. 2, Applied Sci. Pub., 1987, pp. 2.70-2.81
71. H. J. Frost, M. F. Ashby, Deformation Mechanism Maps, Pergamon Press, Oxford, 1982, p. 26.
72. E. A. Starke Jr., J. A. Wert, High Strength Powder Metallurgy Aluminum Alloys II, Ed. G. S. Hildeman, M. J. Koczack, AIME, 1986, pp. 3-23.
73. R. M. German, Powder Metallurgy Science, 2nd Ed., MPIF, Princeton, 1994, pp.192-240.
74. M. F. Ashby, Acta Metall., 22, 1974, pp. 275-289.
75. F. B. Swinkels, M. F. Ashby, Acta Metall., 29, 1981, pp. 259-281.

Chapter 3 Al-Fe-Si Material System

Because significant amounts of Fe and Si impurities are present in all commercial Al alloys, the Al-Fe-Si ternary system is of technological importance. As a result, numerous studies have been performed to try and completely understand this system [1-8]. Unfortunately, there is a general lack of agreement on many of the reactions and ternary phases which are formed. Some of the confusion is rooted in the fact that numerous metastable phases are easily formed as opposed to equilibrium phases. Another area of confusion is that many of the intermetallic compounds have large unit cells with very complicated crystal structures. This leads to difficulty in identification by standard x-ray or electron diffraction.

Of the many reviews of the Al-Fe-Si system, probably the most comprehensive are those of Rivlin and Raynor [1-3]. However, even these reviews leave many questions about the crystallographic information of many phases. Table 3 lists all of the confirmed solid phases, both equilibrium and metastable, which are present at various temperatures in the Al-Fe-Si system. As is easily seen, compiling thermodynamic information or performing calculations with such a large number of phases is a daunting task.

3.1. Binary Systems

In all three cases, the binary diagrams are very well understood. Each system will be reviewed for future reference to experimental results.

3.1.1 Al-Si System

The Al-Si system is a simple eutectic system containing two phases, fcc Al and diamond cubic Si. The binary phase diagram is shown in Fig. 7. Solubility of Si in Al is approximately 1.5 at% at the eutectic temperature of 577°C [9]. The solubility of Al in Si is extremely limited. Most authors quote it as being less than 0.1 at% [1]. There are several factors which are important in predicting whether a binary system will have extensive solid solubility. They should have the same crystal structure, similar atomic radii, a small difference in electronegativities and a similar electron valence structure. These are commonly referred to as the Hume-Rothery rules for substitutional solid solution. Values for these determining factors are listed for the Al-Fe-Si system in Table 4. In the case of Al and Si, the crystal structures are the most important determining factor. Aluminum is fcc with a coordination number of 12. Silicon is diamond cubic with a coordination number of 4. By attempting to substitute Si in Al or Al in Si leads to a highly undesirable situation for either of these atoms with Si attempting to bond with 12 nearest Al neighbors and Al attempting to bond with only 4 nearest Si neighbors. This explains the extremely limited solid solubility in this system.

Table 3. Crystallographic Data for Phases Formed in the Al-Fe-Si System

	Phase Name(s)	Crystal Symmetry	Lattice Parameters (A)	Reference
1.	Al	fcc	4.04	9
2.	θ-Al$_3$Fe Al$_{13}$Fe$_4$, (Al, Si)$_3$Fe	C-centered monoclinic	a=15.49, b=8.08, c=12.48, β=107.75°	9,10
3.	Al$_m$Fe (metastable)	body centered tetragonal	a=8.84, c=21.6	11
4.	Al$_6$Fe (metastable)	C-centered orthorhombic	a=6.49, b=7.44, c=8.79	9
5.	Al$_x$Fe (metastable)	-	-	11
6.	Al$_9$Fe (metastable)	monoclinic	a=8.9, b=6.35, c=6.32, β= 93.4°	9
7.	η-Al$_5$Fe$_2$	orthorhombic	a=7.68, b=6.4, c=4.2	9
8.	ζ-Al$_2$Fe	-	-	9
9.	ε-Al$_3$Fe$_2$	cubic	-	9
10.	β2-AlFe	ordered cubic B2	a=2.909	9
11.	β1-AlFe$_3$	ordered cubic DO3	a=5.79	9
12.	αδ-Fe	bcc	a=2.8665, a=2.9323	9
13.	γ-Fe	fcc	a=3.647	9
14.	β2-Fe	ordered cubic B2	a=2.866-2.81	9
15.	β1-Fe$_3$Si	ordered cubic DO3	a=5.66	9
16.	β3-Fe$_2$Si	-	-	9
17.	κ-Fe$_5$Si3 (η)	hexagonal	a=6.755, c=4.72	9
18.	ρ-FeSi (ε)	cubic B20	a=4.49	9
19.	ωh-FeSi$_2$-h	tetragonal	-	9
20.	ωl-FeSi$_2$-l (ζ)	tetragonal	a=2.69, c=5.133	9
21.	Si	cubic A4 (diamond cubic)		9
22.	Al$_{12}$Fe$_6$Si$_5$ (K$_2$, τ$_2$, γ)	cubic	a=16.03	1
23.	Al$_{12}$(Fe,TM)$_3$Si (K$_5$, α$_1$, C, τ$_5$) (stable with TM)	cubic	a=12.56	10
24.	AlFeSi (q1, α“)	C-centered orthorhombic	a=12.7, b=36.2, c=12.7	11
25.	q2-AlFeSi	monoclinic	a=12.5, b=12.3, c=19.3, β=109°	11
26.	α-Al$_8$Fe$_2$Si (α‘)	hexagonal	a=12.3, c=26.2	12
27.	Al$_9$Fe$_2$Si$_2$ (K$_6$, β, τ$_6$)	monoclinic	a=6.12, b=6.12, c=41.5, β=91°	1
28.	Al$_3$FeSi (γ) (metastable)	C-centered monoclinic	a=17.8, b=10.25, c=8.9, β=132°	12
29.	Al$_4$Si$_2$Fe, Al$_3$FeSi$_2$, (K$_4$,δ, τ$_4$,)	tetragonal	a=6.16, c=9.49	1

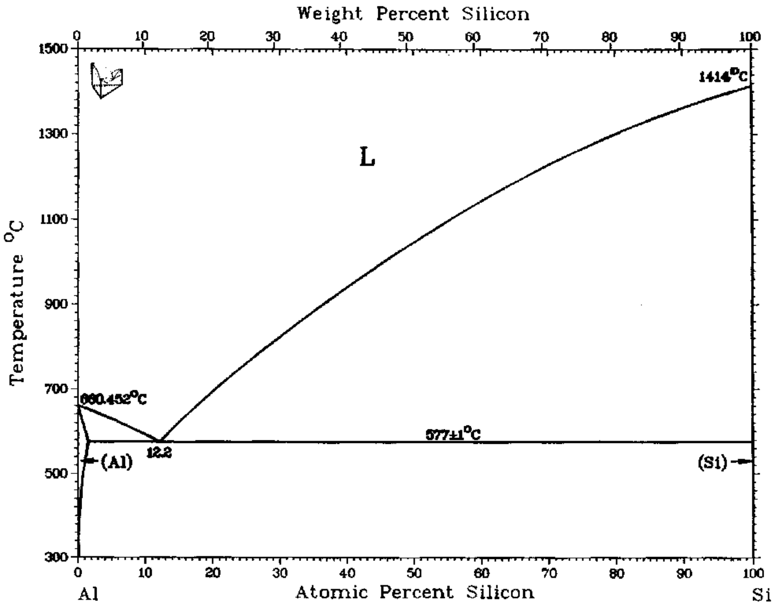

Fig. 7. Al-Si binary phase diagram [13].

Table 4. Hume-Rothery rule values for the Al-Fe-Si system

	Al	Fe	Si
Crystal Structure	fcc	bcc	diamond cubic
Coordination Number	12	8	4
Atomic Radius (A)	1.43	1.24	1.18
Valence	3	2	4
Electronegativity	1.5	1.7	1.8

3.1.2. Al-Fe System

The Al-Fe system is much more complex than the Al-Si system. The binary phase diagram is shown in Fig. 8. The system forms numerous equilibrium intermetallic phases as well as several metastable phases. Solid solubility of Al in Fe is extensive and reaches 45 at% at 1310°C. Solid solubility of Fe in Al, however, is extremely limited and estimated at less than 0.1 at% at 600°C. The explanation of solid solubility is slightly more complicated in the Al-Fe system. An appreciable amount of Al is soluble in Fe while little Fe is soluble in Al. W. Hume-Rothery et. al. noticed a trend whereby, other things being equal, it is common for elements with a lower valence to dissolve elements having a higher valence than vice versa [14]. An excess of electrons present in the higher valence element atoms is a more favorable situation for the dissolving species. In the Al-Fe case, Table 4 shows the electronegativity and atomic size are very similar while the valence of Fe is less than Al.

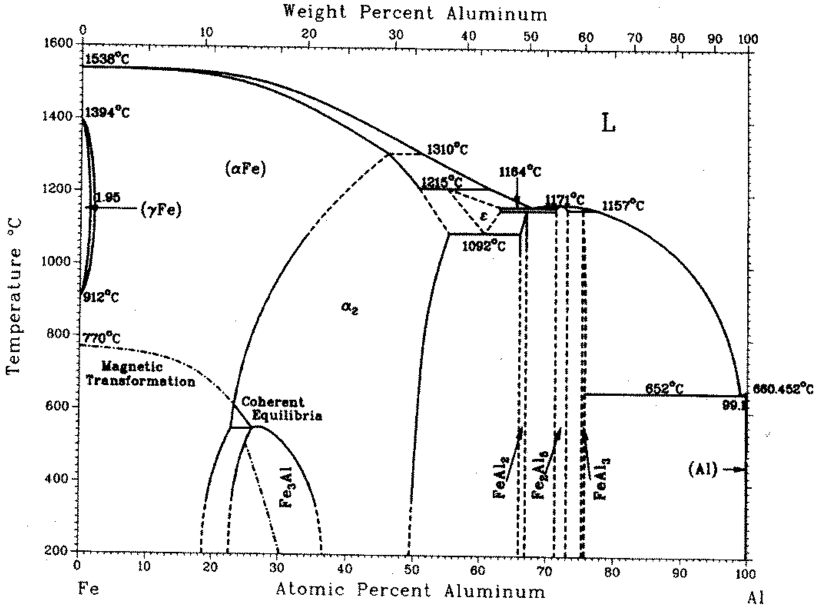

Fig. 8 Al-Fe binary phase diagram [13].

The Fe-Al system contains two ordered structures, Fe_3Al and FeAl, which form from the Fe rich solid solution. The system also contains four equilibrium and four metastable intermetallic compounds. These are all listed in Table 3. Of all of these phases, the most important for our work are those on the aluminum rich side, specifically Al_3Fe.

3.1.3 Fe-Si System

The Fe-Si system is similar in complexity to the Al-Fe diagram. The binary phase diagram is shown in Fig. 9. Solid solubility of Si in Fe extends to approximately 20 at% at 1300°C. The solid solubility of

Fe in Si is negligible. The solid solubility scheme is similar to the Al-Fe system. It can also be described by the Hume-Rothery observation of the lower valence Fe being able to dissolve the higher valence Si. In addition to the two solid solutions, the system contains two ordered phases and 5 additional intermetallic phases. Because most this experimental work was performed in the Al rich region of the ternary system, complete experimental results for this system were not researched.

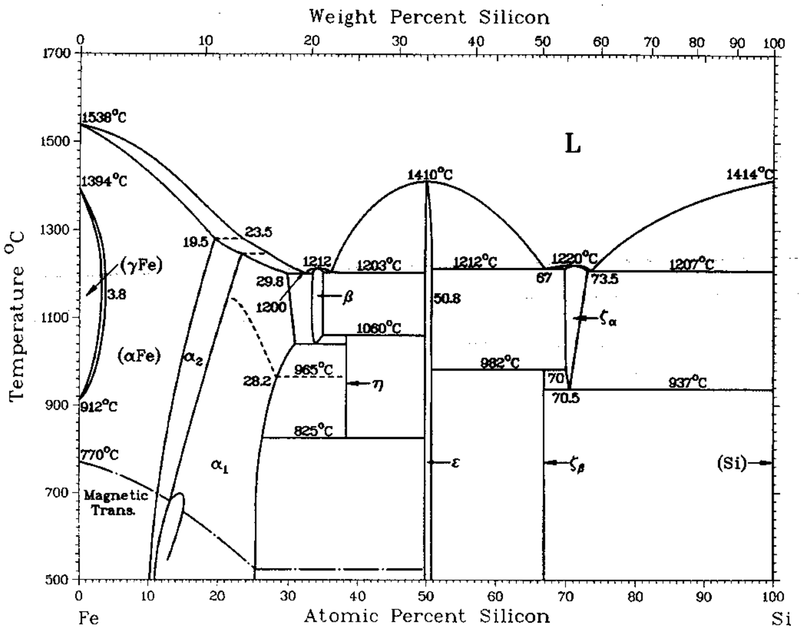

Fig. 9 Fe-Si binary phase diagram [13].

3.2. Ternary System

As already stated, the ternary system has been a source of numerous contradictory reports. This should come as no surprise based upon the complexity of the binary diagrams and the phases which are formed in them. Much of the confusion rises form factors such as supercooling, incomplete reactions and metastability. Fortunately for the present work, most studies are confined to the Al rich alloys. This builds confidence in the results of that section of the diagram. Of the reported ternary phases, six are very well understood and easily confirmed. Some authors have reported as many as ten ternary phases.

Eight ternary phases are listed in Table 3. One of the listed phases is metastable. One of the listed phases, $Al_{12}(Fe, TM)_3Si$, is a cubic phase which is only stable if a small amount of transition metal (TM) impurity is present [1]. This phase is commonly reported in the literature as being a pure ternary phase. The commonly accepted equilibrium diagram at room temperature is shown in Fig 10. The phases listed in the diagram are similar to those listed in Table 3. Because of numerous notations and a range of compositions for each compound, it may be difficult to identify a phase without some persistent and careful research.

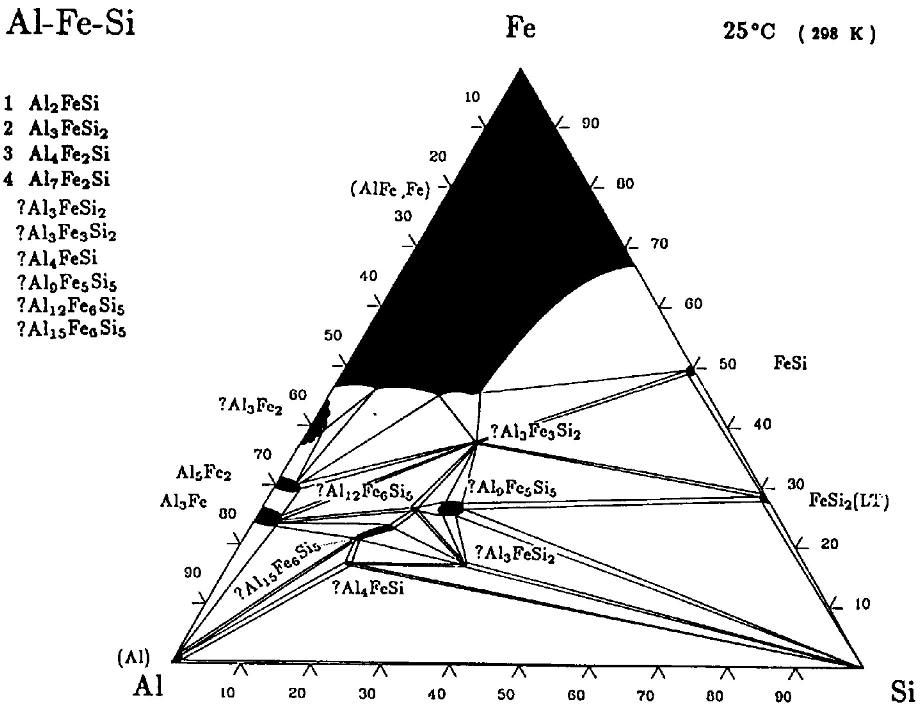

Fig. 10 Al-Fe-Si isothermal ternary diagram at 25°C [15].

The Al-Fe-Si ternary system has traditionally been known as a source of confusion and controversy. Although this work was concentrated on a small region in the Al rich corner, the work lends evidence to the accuracy of the currently accepted ternary equilibrium diagram. In addition, it is encouraging that in the binary systems and the ternary system, the experiments led to the formation of equilibrium phases as opposed to metastable phases which is the case in much of the literature.

References

1. G. V. Raynor and V. G. Rivlin, *Phase Equilibria in Iron Ternary Alloys*, Instit. of Met., London, UK, 1988, 122-139.
2. V. G. Rivlin and G. V. Raynor, Int. Met. Rev., no. 3, 1981, 133-152.
3. G. Rivlin, J. Less Common Met.,vol. 114, 1985, 111-121.
4. J. C. Anglezio, C. Servant and I. Ansara, Calphad, vol. 18, no. 3, 1994, 273-309.
5. L. A. Bendersky, A. J. McAlister and F. S. Biancaniello, Met. Trans., vol. 19a, 1988, 2893-2900.
6. S. K. Das, *Intermetallic Compounds: Principles and Practice Vol. 2,* Ed. J. H. Westbrook and R. L. Fleisher, J. Wiley & Sons, Chichester, UK, 1993, 175-198
7. L. A. Bendersky, Key Engineering Materials, vol. 44&45, 1990, 127-134.
8. Y. Langsrud, Key Engineering Materials, vol. 44&45, 1990, 95-116.
9. W. B. Pearson, *Handbook of Lattice Parameters of Metals and Alloys*, Pergamon Press, 1958.
10. V. Stefaniay, A. Griger, T. Turmezey, J. Mat. Sci., vol. 22, 1987, 539-546.
11. P. Liu, T. Thorvaldsson and G. L. Dunlop, Mat. Sci. Tech., vol. 2, 1986, 1009-1018.
12. D. Munson, J. Inst. Met., vol. 95, 1967, 217-219.
13. *Binary Alloy Phase Diagrams*, Ed. T. B. Massalski, 2nd Ed., ASM Int., Materials Park, OH, 1990.
14. W. Hume-Rothery, G. W. Mabbott, and K. M. Channel-Evans, Phil. Trans. Roy. Soc., vol. 233A, 1934, 44.
15. *Handbook of Ternary Alloy Phase Diagrams*, Eds. P. Villars, A. Prince and H. Okamoto, ASM Int., Materials Park, OH, 1995.

Chapter 4 Experimental Techniques

4.1 Production of Precursor Powders via Mechanical Alloying

Aluminum, Fe_2O_3 , and SiO_2 powders with purities of 99.8 at.% each were placed in a 65 cm^3 stainless steel mixing vial and milled in a SPEX™ 8000 mixer/mill. Chemistry of the powders was varied between 1.75 and 43 mol% oxide powder with the balance being aluminum. Stearic acid (2 wt.%) was added to the vial as a process control agent to prevent powder from adhering to the vial. The powder charge was maintained at approximately 10g. The charge ratio (mass of the milling media to the mass of the powder mixture) was varied between 1:1 and 6:1 by changing the number of milling balls in the vial. Between 2 and 11 stainless steel 11-mm-OD balls were used. The vials were sealed in an argon-filled glove box to minimize oxidation.

4.2 Initiation of Displacement Reactions

4.2.1 Initiation via Mechanical Alloying

Under certain conditions, a thermite reaction would occur during mechanical alloying. To study this, samples were milled for times of 0.5 – 50 hrs. At 0.25 hr increments, the samples were analyzed using x-ray diffraction to determine if reactions had occurred.

4.2.2 Initiation via Heat Treatment

Thermite reactions could also be initiated via heat treatment. For these experiments, samples were mechanically alloyed for fixed times. The samples were then heat treated at 400° - 600°C under argon. X-ray analysis was performed to determine if reactions had occurred.

4.2.3 Thermal Analysis of Reactions

As a means to study reaction temperatures and reaction kinetics, differential thermal analysis (DTA) was performed on the milled powders using a Perkin Elmer DTA-1700. An argon purge with a 40ml/min flow rate was utilized. A range of heating rates from 2-20°C/min were used.

4.2.4 X-ray Analysis

Confirmation of reaction and analysis of phases present was performed using a Scintag X-ray diffractometer with a liquid nitrogen cooled germanium detector. Theta-theta scans were performed using Cu-Kα radiation.

4.2.5 Thermodynamic Predictions for Reactions

Thermodynamic calculations were performed using a FORTRAN based SOLGASMIX software. The molar quantities of the starting phases along with thermodynamic information were put into the program. The equilibrium phases which should be present at a given temperature and pressure were then determined. The calculations were based upon the experimental parameters used during mechanical alloying. Identical volumes of Al, Fe, O and Ar as those used experimentally were put into the program. The equilibrium phases were computed at temperatures of 300, 873, and 1273°K and atmospheric pressure. In addition, a constant volume calculation was performed by using the parameters of the SPEX mill mechanical alloying equipment.

4.3 Densification of Reacted Powders

4.3.1 Cold Pressing and Annealing

Following milling and reaction via annealing, powder samples were cold pressed in a 2.54 cm die at 620 MPa using a Tinius-Olsen press. Samples were then annealed under argon at 550°C for 1 hour.

4.3.2 Extrusion

Al-1.75mol% Fe_2O_3 1/2 hr mill and the Al-3.5mol% samples milled for 1/2 and 5 hours were reacted by annealing at 550°C for 5 hours. The Al-1.75mol% Fe_2O_3 5 hour milled sample had to be reacted at 600°C for 5 hours. The four powder samples were each encapsulated in 6061 aluminum cans. The cans were vacuum degassed at 500°C for 4 hours and extruded at 500°C with a 12:1 extrusion ratio. Extrusions were performed in the Metals Processing Laboratory at Oak Ridge National Lab.

4.4 Analysis of Bulk Samples

4.4.1 Optical Microscopy

Optical microscopy was performed on all powder and densified samples using a Jena Neophot 21 microscope. Samples were etched using a mixture of 10 vol %HF and water.

4.4.2 Electron Microscopy

Scanning electron microscopy was performed using a JEOL Superprobe 442 equipped with EDXS and both secondary and backscatter electron detectors. An accelerating voltage of 20 keV was used.

Transmission electron microscopy was performed using a Philips EM-420 scanning-transmission electron microscope with an accelerating voltage of 100keV. Samples were prepared by grinding a thin foil of pressed and sintered material to a thickness of ~75 microns. 3 mm discs were punched from the foil. A Gatan dimple grinder was then used to thin the center of the sample to ~40 microns. A Gatan Duo-mill ion mill was used to thin the samples for microscopy.

4.4.3 Hardness Testing

Rockwell indentation hardness and Knoop microhardness readings were performed on all densified samples. For Rockwell, tests were performed using the A and F scales with a diamond indenter. For Knoop microhardness, a 500 gf load was used with 15 second hold at load.

4.4.4 Mechanical Testing

Tensile tests were performed on specimens machined from the extruded samples. Tests were performed using an Instron machine using a strain rate of 0.026/min.

4.4.5 Chemical Analysis

Bulk densified samples were analyzed for composition of aluminum, iron, silicon, carbon, and oxygen.

4.4.6 Density Measurements

Archimedian density was measured on the extruded samples according to ASTM B311.

Chapter 5 Displacement Reactions: Results and Discussion

5.1 Reactions Initiated by Mechanical Alloying

Mechanical alloying (MA) was used to blend Al with Fe_2O_3 or SiO_2. It was found that displacement reactions could be initiated simply with MA for the Al-Fe_2O_3 system. Fig. 11 shows the ball milling results for the 15 and 20 mol% Fe_2O_3 samples. As the concentration of Fe_2O_3 is decreased, the "milling reaction time" is increased. Complete reactions in the Al-Fe_2O_3 system occurred in only a few seconds and the "milling reaction time" was considered as an incubation and completion time for the reaction. Initiation and completion of a reaction was determined by x-ray analysis of samples taken from the powder charge at regular time intervals. Representative x-ray diffraction patterns for 15 mol% Fe_2O_3 samples before and after reaction are shown in Fig. 12. The primary phases present after reaction are Al, $Al_{13}Fe_4$, and α-Al_2O_3. Below a critical composition, no reaction was observed during milling. The critical value lies between 10 and 15 mol% Fe_2O_3. There appears to be a minimum milling reaction time of ~2 hrs for the 15 and 20 mol% Fe_2O_3 specimens. More importantly, an exponential relationship develops between the charge ratio (ratio of the milling media mass to the powder mass) and the milling reaction time. As the charge ratio decreases, the milling reaction time exponentially increases. A best fit to the data can be described by the equation:

$$t = a + be^{-r} \tag{5.1}$$

were t is milling reaction time, r is the charge ratio and a & b are constants.

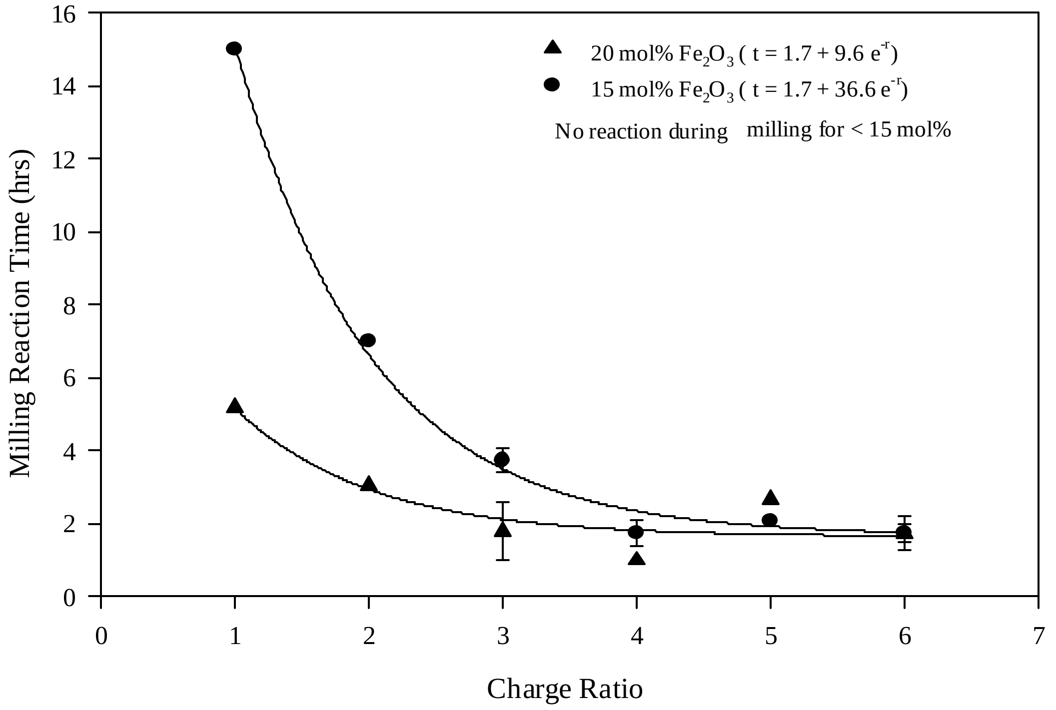

Fig. 11. Ball milling time vs. charge ratio for Al - Fe_2O_3.

A similar relationship was shown by Schaffer and McCormick to occur for the initiation of reactions in the CuO-Fe system [1]. They contended that combustion during milling occurred when the ignition temperature of the powder was reduced to the temperature which occurs locally at impacts between balls. They stated that the charge ratio did not affect the reaction temperature, it only changed the time required to achieve that temperature. Also, they concluded the product of charge ratio and milling reaction time was a constant. The results from Fig. 11 show that the product of charge ratio and milling reaction time are not a constant and that a different mechanism than described by Schaffer must be occurring.

Schaffer and McCormick have also shown that actual physical changes in powder particles can be produced by modifying either the charge ratio or milling time. Both increased charge ratio and milling time result in a more rapid reduction of powder particle size and distribution of starting components [1]. As either milling time or charge ratio increases, the amount of energy which is imparted into the powder charge is increased, yielding an increased absorption of energy per particle [1]. The increased energy absorption results from a higher number of collisions between milling media and powder particles. In a model developed by Aikin et al. [2] for metal-metal alloying studies, it is believed that it is the energy absorption alone which determines the powder characteristics. In the study by Schaffer and McCormick [1] on chemical reactions during MA, it was determined that it was both the energy absorbed and the number of collisions which determine the powder characteristics and the resulting reaction kinetics.

The occurrence of a solid state displacement reaction is enhanced by mechanical alloying in three important ways. As milling time or charge ratio are increased, the reactant particle size is reduced leading to an increase in the overall surface area. The increased surface area means more interfacial contact for the different reactant species. In addition, the continued MA repeatedly exposes new unreacted surfaces with its blending and kneading action. As a result, barriers produced by product phases are reduced. Lastly, MA produces numerous defects in metallic materials. The massive quantities of defects enhance diffusion in MA processed powders [3]. In general, as milling time or charge ratio is increased, the reactivity of the mixture is increased. It has been stated by Forrester and Schaffer [4] that reactions during MA are controlled by diffusion down short-circuit pathways. Along similar lines, we can state that the reactions shown in Fig. 11 are being controlled by enhanced diffusion as the result of deformation induced defects in the powders. Some evidence of this can be seen in Fig. 13 which shows the effective crystallite size vs. milling time for aluminum from a mixture of Al - 3.5 mol% Fe_2O_3 which was milled at a 6:1 charge ratio. Effective crystallite size was calculated from x-ray diffraction of aluminum (110) peaks using the Scherrer formula and accounting for instrumental line broadening [5]. Direct examination of 15 or 20 mol% Fe_2O_3 powders at long milling times was not allowable due to the pyrophoric nature of those blends. In the figure, the effective crystallite size is rapidly reduced with milling time. A decreased effective crystallite size is associated with a decreased grain, subgrain or cell size [5]. It is the increase in boundary area resulting from the formation of additional grains or subgrains which is a route for short-circuit diffusion. The results shown in Fig. 13 correspond well with the results of similar experiments performed on the CuO-Fe system by Schaffer and McCormick [1].

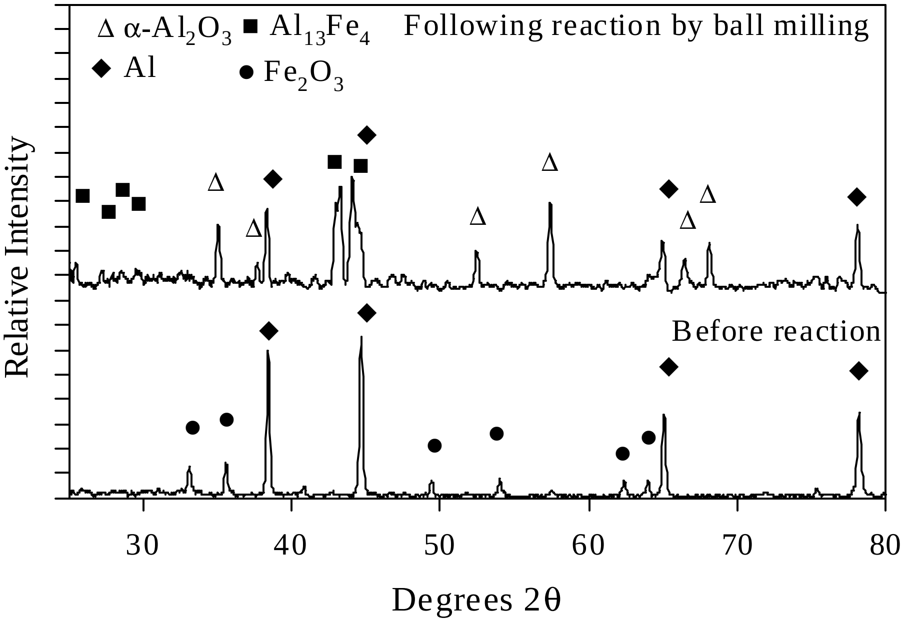

Fig. 12 Representative x-ray diffraction patterns for 15 mol% Fe_2O_3 samples before and after reaction by mechanical alloying.

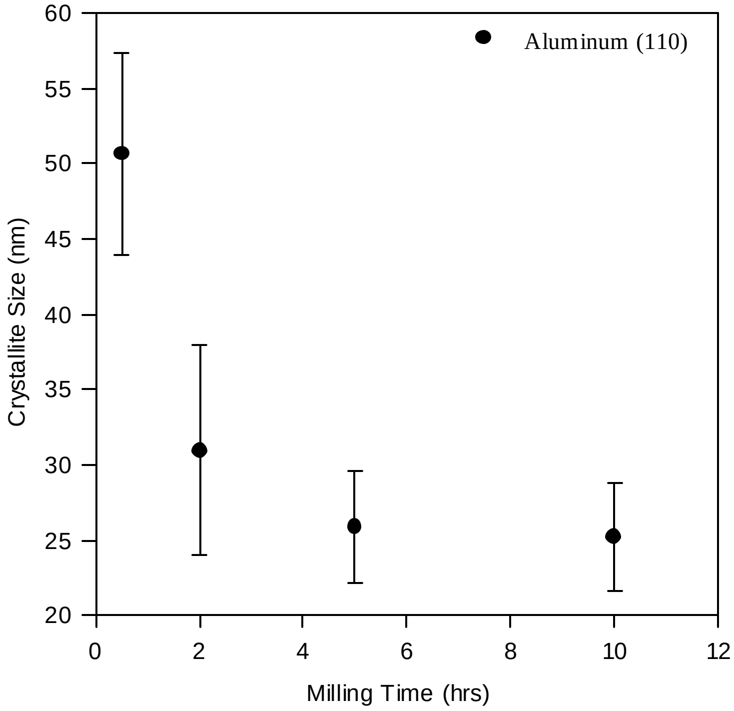

Fig. 13. Effective crystallite size calculations at various milling times for Al (110) peaks from a mixture of Al-3.5 mol% Fe_2O_3 milled at a 6:1 charge ratio.

Although work by Hida and Lin demonstrated that reactions could be initiated in mixtures of Al and SiO_2 [6], the current work could not repeat those results. Mixtures of Al with 15, 20 and 43 mol% SiO_2 were milled for times up to 50 hrs with no evidence of a displacement reaction. The reactions could only be initiated by subsequent heat treatment. One explanation for the difference between this work and the work of Hida and Lin could be the MA equipment. Hida and Lin utilized an attritor type mill which uses a shearing action to mix the powders. In the current work, a SPEX-type shaker mill was used to mix the powders. Impacts in a shaker mill are predominantly compressive in nature and may have a different effect on reaction initiation.

5.2 Reactions Initiated by Heat Treatment

5.2.1. Al-Fe_2O_3

In addition to reactions initiated by ball milling, reactions were also initiated by thermal means. To study the reactions, differential thermal analysis (DTA) was used. Powder samples containing various amounts of Fe_2O_3 (1.75, 3.5, 7.5, 10, 15, and 20 mol% Fe_2O_3) were mechanically alloyed using two different charge ratios (1:1 and 6:1) for 1/2 hr. DTA scans for the 7.5 -20 mol% Fe_2O_3 at a 10°C/min heating rate and a 1:1 charge ratio are shown in Fig. 14. It can be seen that as the composition of Fe_2O_3 is increased, the exothermic reaction temperatures are increased. The increase in reaction temperature is again explained as resulting from effects of the mechanical alloying process. During the MA process, the aluminum powders are being fractured and welded together while the Fe_2O_3 is being fractured and blended into the more ductile aluminum. The two materials eventually become very intimately mixed such that a high amount of interfacial contact between the reactants is achieved. Neglecting short-circuit diffusion paths and focusing on the actual average diffusion distance between the two different reactant particles, as more interfacial contact is achieved, the reactions should be propagated more readily [7]. As Fe_2O_3 percentages increase, the efficiency and completeness with which the oxide can be blended into the matrix is reduced. Therefore for higher percentage mixtures, the reaction is not as easily propagated and the exothermic reaction temperature is increased. The endothermic peak in the figure indicates the melting temperature of the aluminum.

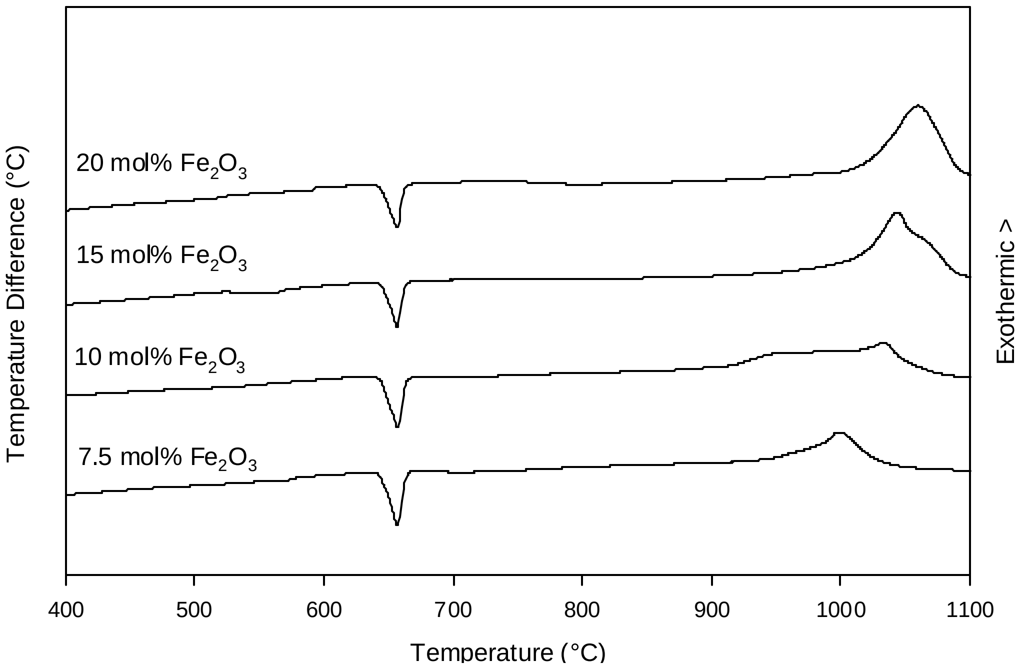

Fig. 14. Differential thermal analysis of the 1:1 charge ratio samples milled for 0.5 hr heated at 10°C/min.

Fig. 15 shows the DTA scans for the 6:1 charge ratio samples. In these samples, there is also an upward shift of the reaction temperature with the increasing Fe_2O_3 concentration. It can be explained similarly to the 1:1 charge ratio samples. As the concentration of Fe_2O_3 increases, the mixing becomes more dilute and reaction temperature increases. Comparing the 6:1 ratio with the 1:1 results, a dramatic decrease in the reaction temperature is seen for the 6:1. As expected, the higher charge ratio allowed for better and more complete mixing thus leading to the reaction temperature decrease. Another observation from Fig. 15 is that the reaction temperature for the three lowest concentrations is preceded by the melting of aluminum. It is surmised that the formation of a small amount of molten aluminum facilitated the reaction.

One major difference between the 1:1 and 6:1 charge ratio DTA scans seems to be the change from a single reaction peak in the 1:1 samples to two reaction peaks for the 6:1 samples. What seems more likely is that for both charge ratios, there are two peaks present. In the 1:1 charge ratio, however, the two peaks may be very close in temperature. As the charge ratio is increased, one of the reactions is more strongly affected by the mechanical alloying process. As a result, a split of the two reaction temperatures is seen.

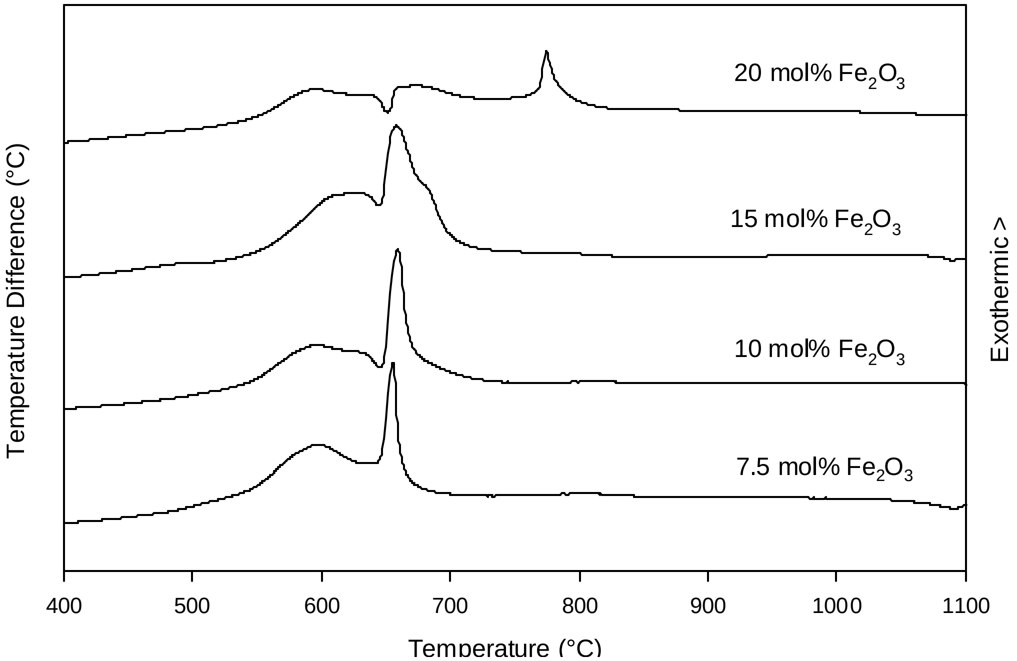

Fig. 15. Differential thermal analysis of 6:1 charge ratio samples milled for 0.5 hr heated at 10°C/min.

If there are two distinct chemical reactions and one is more strongly affected by mechanical alloying, increased charge ratio or increased milling time should lead to a visible change in the reaction peak location as determined with thermal analysis. Figure 16 shows DTA traces for Al-3.5 mol% Fe_2O_3 which was milled at a 6:1 charge ratio for 1/2 hr and 5 hr. It can be seen from the longer milled sample that the lower temperature peak has shifted from ~550°C down to ~225°C. X-ray diffraction performed on specimens heated above the first reaction peaks for the 0.5 and 5hr milled conditions has confirmed that it is the same reaction occurring in both specimens.

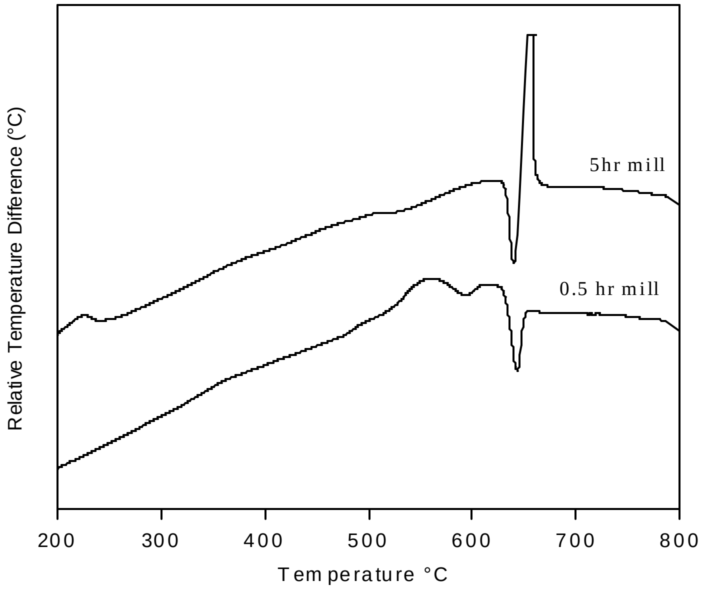

Fig. 16. DTA for 3.5 mol% Fe_2O_3 milled at a 6:1 charge ratio and heated at 5°C/min.

X-ray diffraction has been able to provide valuable information about the nature of the reactions which are occurring during thermal analysis. Powder samples were heated under high purity argon to 500°C, 600°C, and 900°C at 5°C/min and then furnace cooled. Fig. 17a shows x-ray diffraction for Al - 3.5mol% Fe_2O_3 which was milled at 6:1 for 0.5 hrs and then heat treated at 500°C. The dominant phases present are Al, and Fe_2O_3 (hematite). Fig. 17b shows x-ray diffraction for Al - 3.5mol% Fe_2O_3 which was milled at 6:1 for 5 hrs and then heat treated at 500°C. The phases present are Al and Fe_3O_4 (magnetite). Fig. 17c shows x-ray diffraction for Al - 3.5mol% Fe_2O_3 which was milled at 6:1 for 0.5 hrs and then heat treated at 600°C. The dominant phases present are Al and Fe_3O_4 (magnetite). Figure 17d shows x-ray diffraction for Al - 3.5mol% Fe_2O_3 which was milled at 6:1 for 5 hrs and then heat treated at 600°C. The phases present are Al and Fe_3O_4 (magnetite). Figures 17e and 17f show x-ray diffraction for Al - 3.5mol% Fe_2O_3 which was milled at 6:1 for 0.5 and 5 hrs, respectively. Both figures show the dominant phases as Al and $Al_{13}Fe_4$. The results of the x-ray diffraction are summarized in Table 5. From this data, it is believed that the low temperature reaction is the conversion of Fe_2O_3 to Fe_3O_4, and the higher temperature reaction is the reduction of Fe_3O_4 and formation of $Al_{13}Fe_4$.

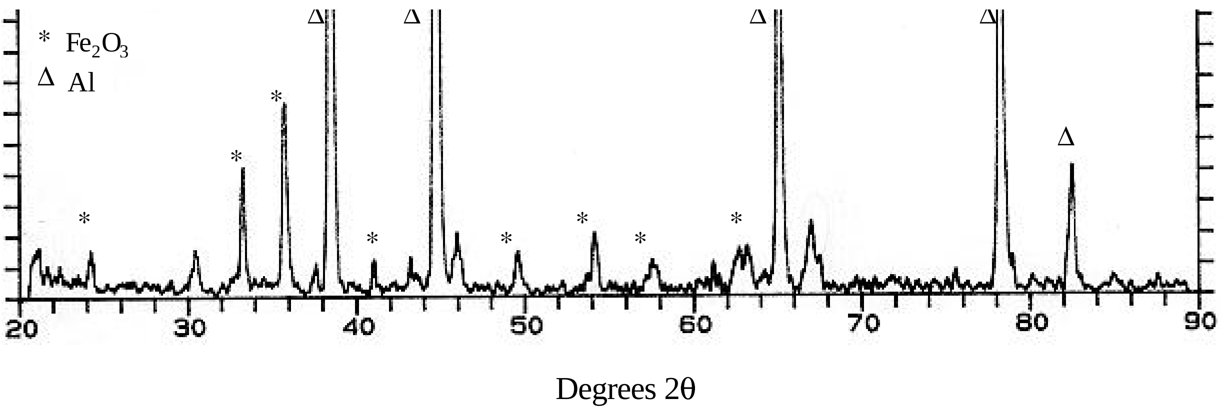

Fig. 17a X-ray diffraction for Al - 3.5mol% Fe_2O_3 which was milled at 6:1 for 0.5 hrs and then heat treated at 500°C

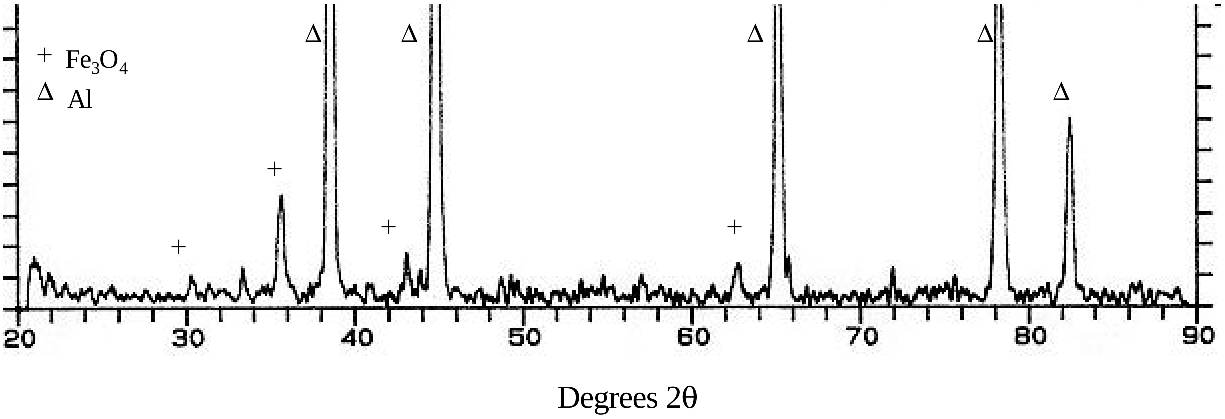

Fig. 17b X-ray diffraction for Al - 3.5mol% Fe_2O_3 which was milled at 6:1 for 5 hrs and then heat treated at 500°C

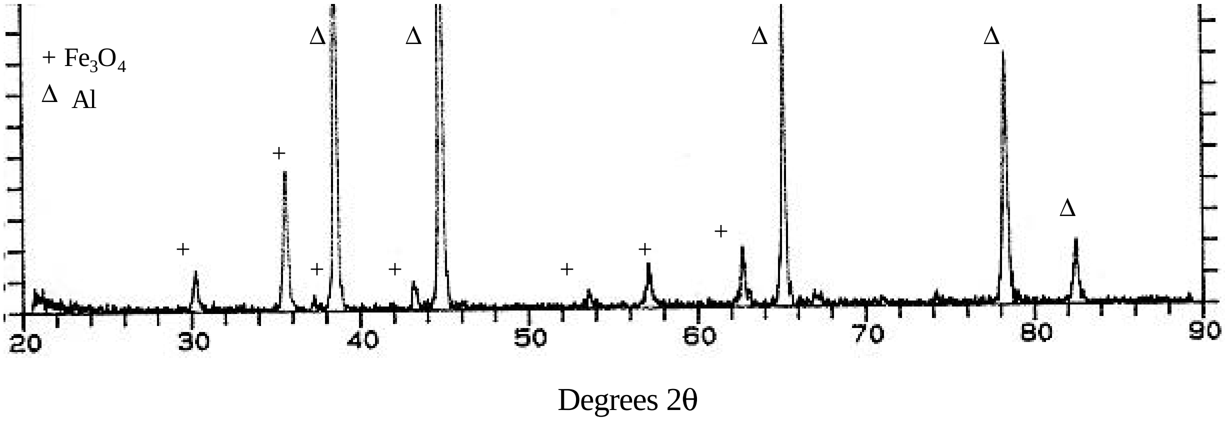

Fig. 17c X-ray diffraction for Al - 3.5mol% Fe_2O_3 which was milled at 6:1 for 0.5 hrs and then heat treated at 600°C

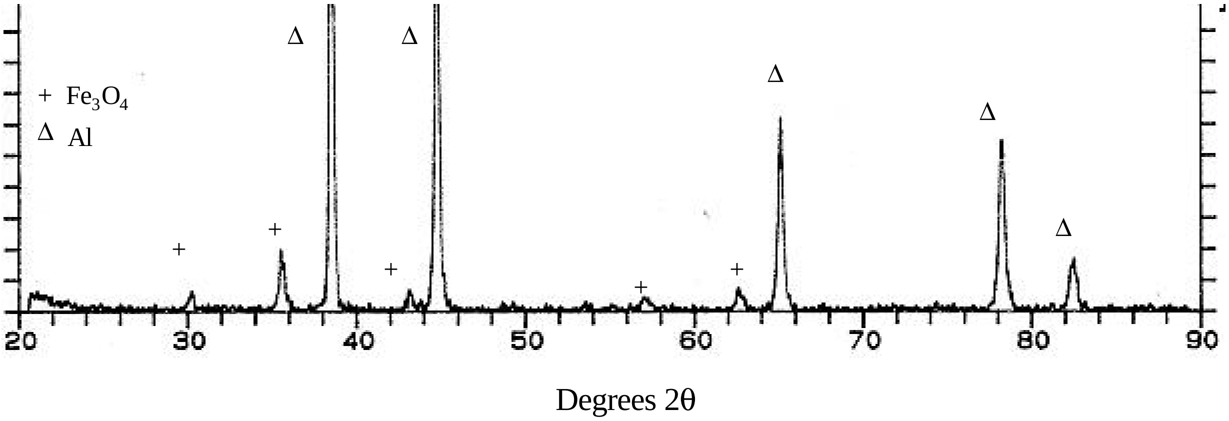

Fig. 17d X-ray diffraction for Al - 3.5mol% Fe_2O_3 which was milled at 6:1 for 5 hrs and then heat treated at 600°C

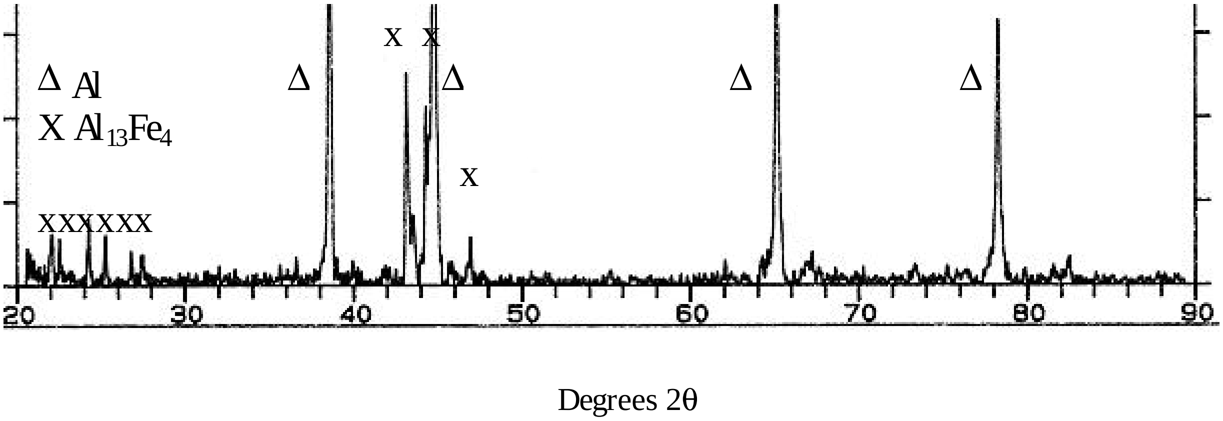

Fig. 17e X-ray diffraction for Al - 3.5mol% Fe_2O_3 which was milled at 6:1 for 0.5 hrs and then heat treated at 900°C

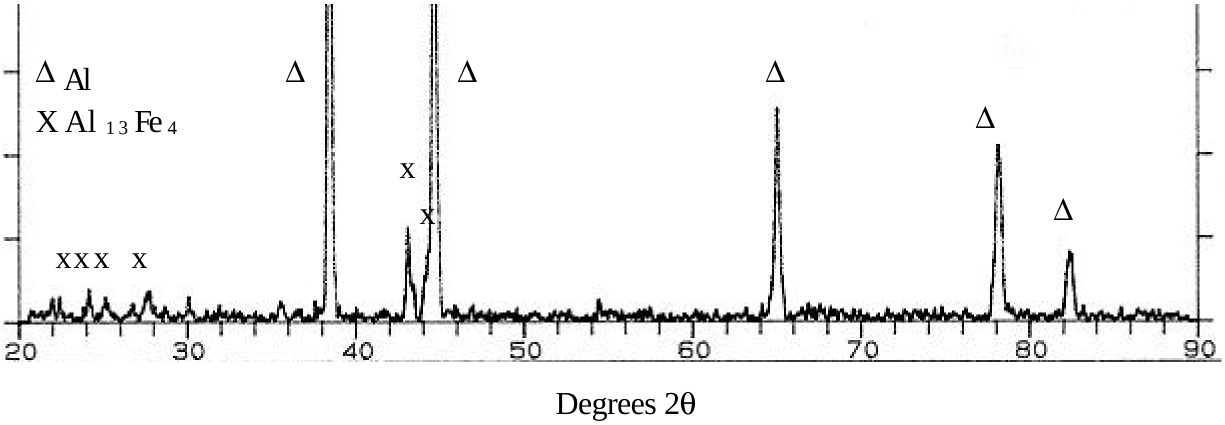

Fig. 17f X-ray diffraction for Al - 3.5mol% Fe_2O_3 which was milled at 6:1 for 5 hrs and then heat treated at 900°C

Table 5. Dominant phases present after various heat treatment temperatures for Al 3.5mol% Fe_2O_3 milled at 6:1 charge ratio. Table summarizes data from Fig. 17.

	Temperature		
	500°C	600°C	900°C
0.5hr mill	Al & Fe_2O_3	Al & Fe_3O_4	Al & $Al_{13}Fe_4$
5 hr mill	Al & Fe_3O_4	Al & Fe_3O_4	Al & $Al_{13}Fe_4$

Kissinger [8] determined that the apparent activation energies of the reactions can be found by performing DTA at different heating rates. By determining the peak locations at the different rates, an Arrhenius plot can be produced. For each reaction, the apparent activation energy can be found from the slope of the line. Figure 18 shows DTA data for Al-3.5mol% Fe_2O_3 milled at 6:1 charge ratio for 0.5 hrs and using heating rates of 2, 5, and 10°C/min. Figure 19 shows the corresponding Arrhenius plots for both 1/2 hr and 5hr milled samples. The corresponding apparent activation energies (Q) are also included in the figure.

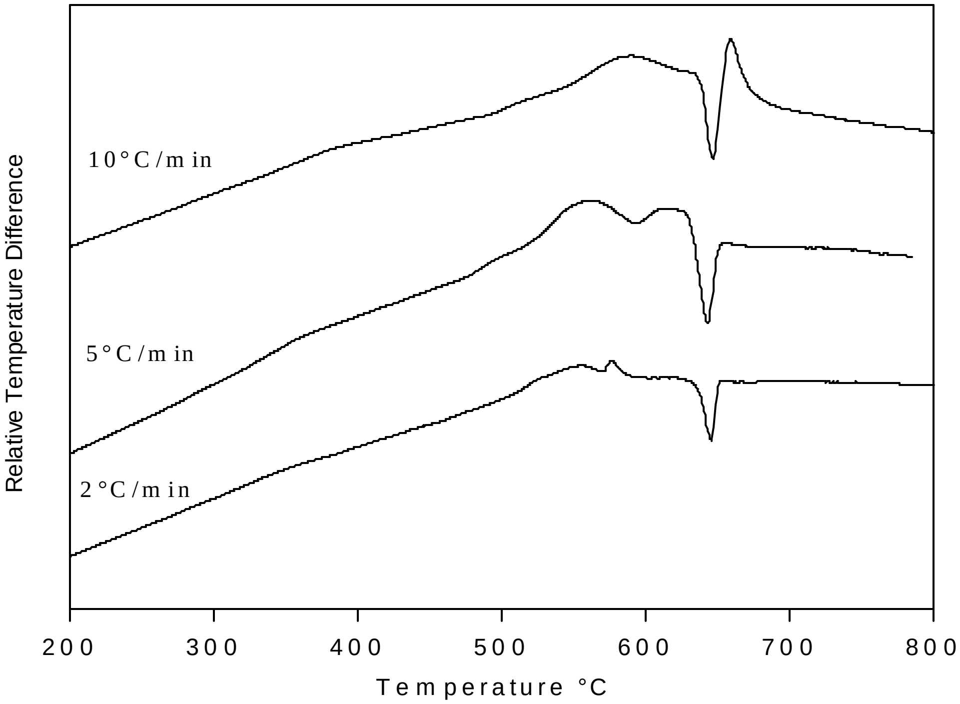

Fig. 18. DTA scans performed at 2, 5, and 10°C/min for Al -3.5mol% Fe_2O_3 which was mechanically alloyed for 0.5 hr with a 6:1 charge ratio.

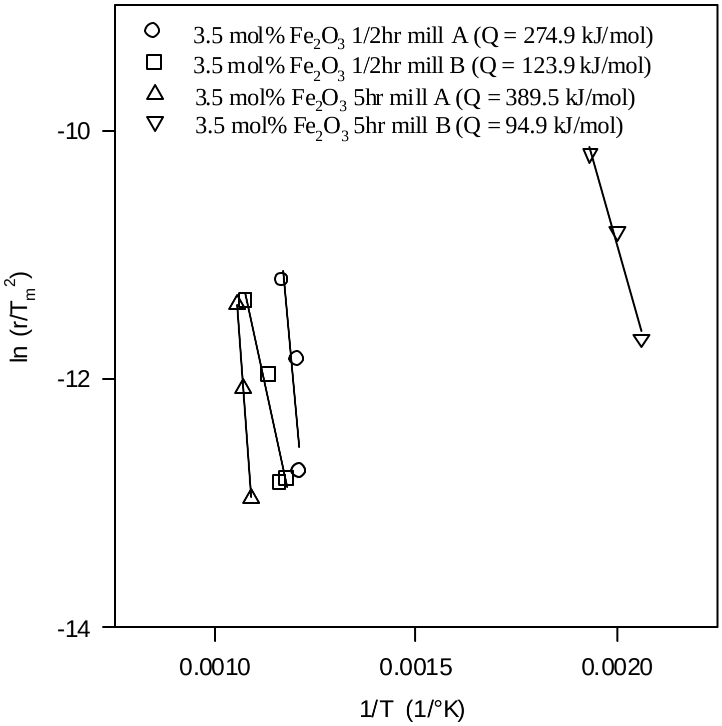

Fig. 19. Arrhenius plots for Al-3.5mol% Fe_2O_3 milled for 0.5 and 5 hrs. Also included are the activation energies (Q) of the reactions. Reaction A corresponds to the high temperature reaction while Reaction B corresponds to the low temperature reaction.

A reduction of the activation energy for the low temperature Fe_2O_3 to Fe_3O_4 reaction from 123.9 kJ/mol at 1/2 hr of milling to 94.9 kJ/mol at 5hrs of milling is a key observation. Forrester and Schaffer [4] saw similar decreases during solid state reduction of CuO by Fe which had been enhanced by mechanical alloying. Their conclusion was that the reduced activation energy was the result of a change in the rate limiting step of the reaction. Namely, that ionic diffusion was increased due to the presence of deformation induced defects in the particles. A similar conclusion can be drawn in this case.

As for the high temperature reactions, it is not completely understood why the activation energy is increasing with increased milling time. It may be that the occurrence of the melting of Al is affecting the ability to accurately measure reaction temperatures. It may also be possible that increased MA milling time is actually inhibiting the reaction. In many cases with combustion-type exothermic reactions, it has been inferred that heat dissipation is important for controlling reaction rates [9]. As the reaction is initiated, a certain amount of heat is required for the reaction to self-propagate. If the heat is rapidly drawn away from the reaction region, the reaction will be inhibited. For the case of 5hr milled samples, the iron oxide reactant is distributed uniformly throughout the Al matrix. Any heat which is formed from a reaction at the iron oxide interface could be rapidly drawn away into the aluminum preventing the reaction from self-propagating.

5.2.2. Al-SiO_2

As previously mentioned, mixtures of Al and 15, 20, and 43mol% SiO_2 were processed using mechanical alloying at a 6:1 charge ratio for times up to 50 hours with no evidence of reaction during milling. Samples of Al - 15mol% SiO_2 milled 5 hrs at 6:1 CR were annealed in argon at 600°C for one hour with a furnace cool. Under these conditions, the displacement reaction could be initiated. Figure 20 shows x-ray diffraction of samples before and after reaction. The product phases following reaction are Al, Si , and α-Al_2O_3.

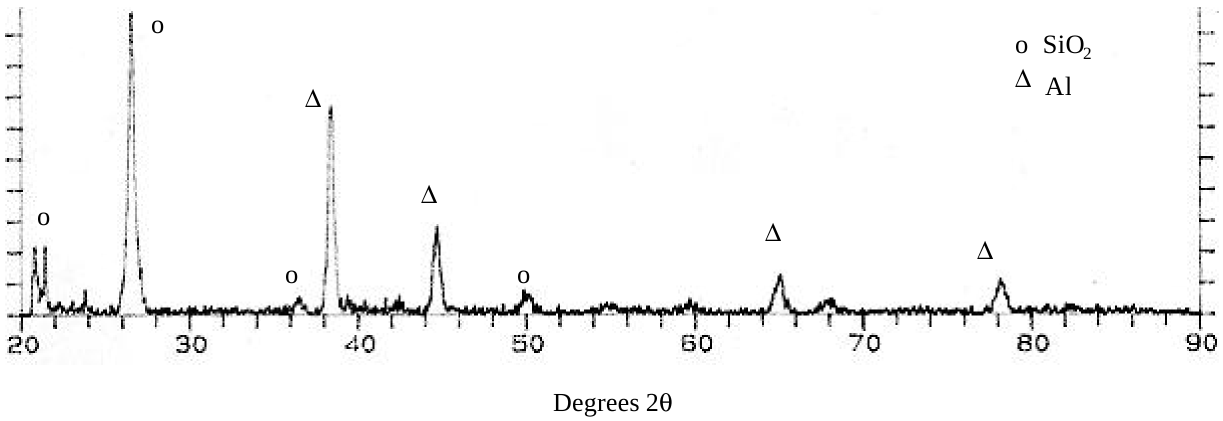

Figure 20a. X-ray diffraction of Al-15mol% SiO_2 milled for 5hrs at 6:1 CR.

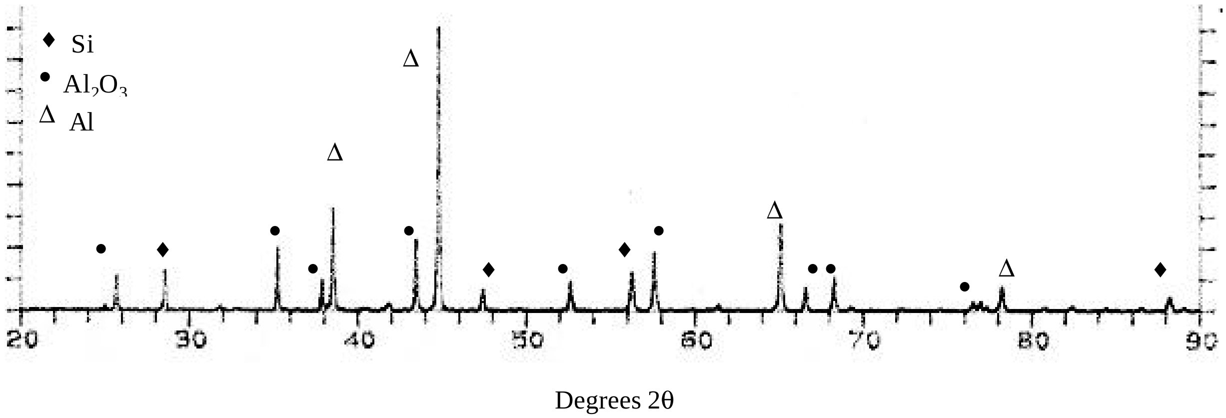

Fig. 20b X-ray diffraction of Al-15mol% SiO_2 milled for 5hrs at 6:1 CR and heat treated at 600°C for 1 hr.

5.3 Thermodynamic Predictions for Reaction Products

In an effort to understand what phases are thermodynamically stable in the Al -Fe_2O_3 material system, calculations were made using the SOLGASMIX-PV program. SOLGASMIX was developed at Oak Ridge National Lab [10] to calculate the equilibrium phases formed in a reaction based upon thermodynamic principles. The program determines the amounts of each stable phase present by minimizing the total Gibbs free energy of the system. By using the program, comparisons can be drawn between calculated equilibrium phases and those formed experimentally.

Table 6 shows the equilibrium amounts of each phase which should be present in the Al-10 mol% Fe_2O_3 system before and after reaction at room temperature (300°K). These amounts are the results of the SOLGASMIX calculations. The results are similar to the experimental results. Both the experimental results and the SOLGASMIX calculations show the formation of the Al_3Fe intermetallic compound along with metallic Al. In addition to the formation of $Al_{13}Fe_4$ and Al, the program predicts the formation of Al_2O_3. The formation of Al_2O_3 should come as no surprise. By looking at the Ellingham diagram for the formation of oxides shown in Figure 21, it is easily seen that the free energy of formation for Al_2O_3 is much lower, at the calculated temperatures, than any of the Fe-O compounds.

Table 6. SOLGASMIX results for 300°K and a constant pressure of 1 atm.

Compound	Amount Before Reaction (moles)	Amount After Reaction (moles)
Ar	1	1
O_2	0.000835	0
Al_2O_3	0	0.0005567
Fe	0.00446	0
Al	0.3058	0.29131
$Al_{13}Fe_4$	0	0.00446

Table 7 shows results of the SOLGASMIX calculations performed at an elevated temperature of 873°K. This approximates the temperature in one of the experimental heat treating operations. The results are similar to the room temperature calculations.

Table 7. SOLGASMIX results for 873°K and a constant pressure of 1 atm.

Compound	Amount Before Reaction (moles)	Amount After Reaction (moles)
Ar	1	1
O_2	0.000835	0
Al_2O_3	0	0.0005567
Fe	0.00446	0
Al	0.3058	0.29131
$Al_{13}Fe_4$	0	0.00446

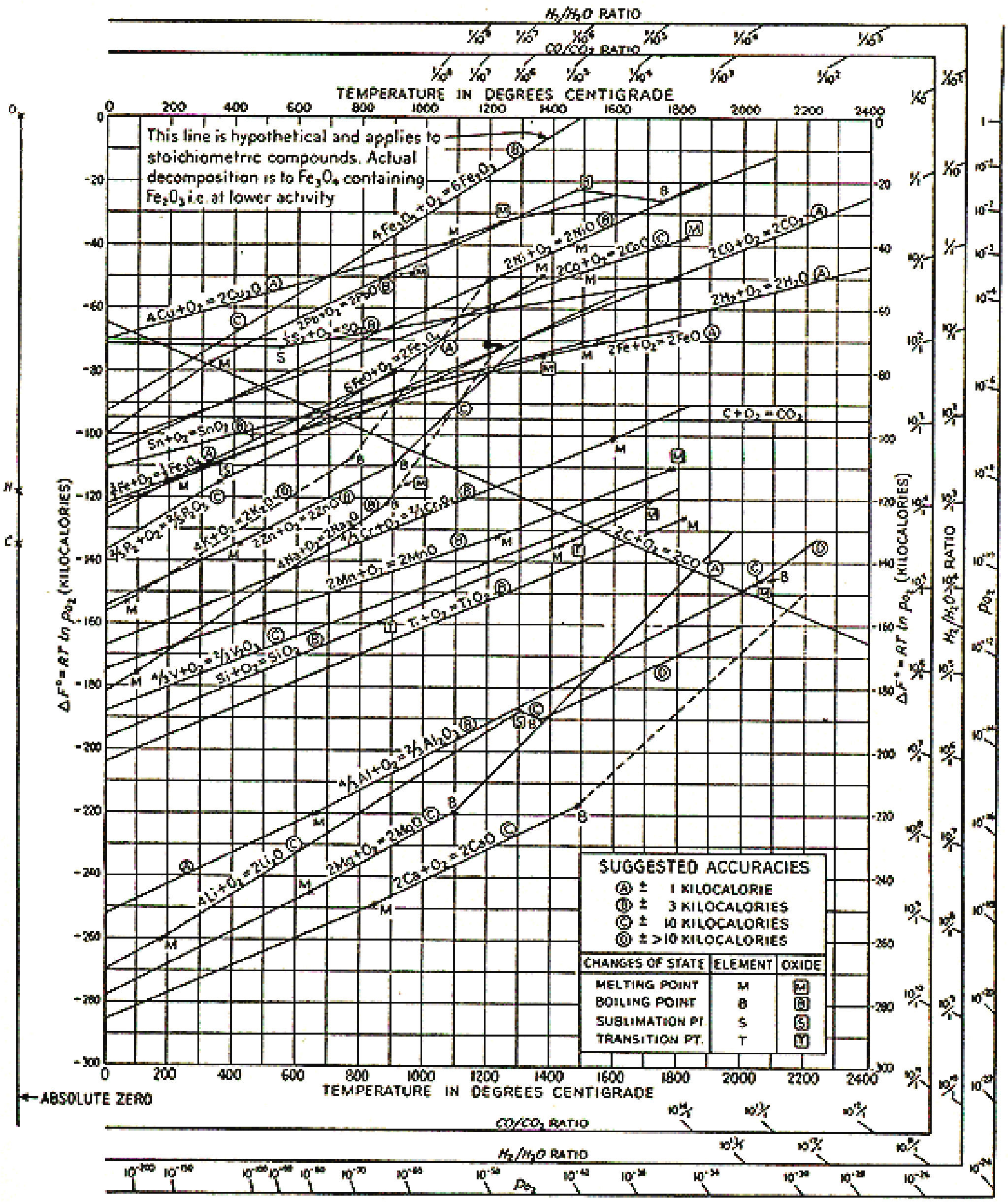

Figure 21. The standard free energy of formation (Ellingham Diagram) of many metal oxides as a function of temperature [11].

Table 8 shows results of the SOLGASMIX calculations performed at 300°K and a constant volume of 65 cm^3 (volume of a SPEX milling vial). This approximates the temperature and volume present during the mechanical alloying operation. The results are identical to the room temperature calculations at constant pressure.

Table 8. SOLGASMIX results for 300°K and a constant volume of 65 cm^3.

Compound	Amount Before Reaction (moles)	Amount After Reaction (moles)
Ar	0.00244	0.00244
O_2	0.000835	0
Al_2O_3	0	0.0005567
Fe	0.00446	0
Al	0.3058	0.29131
$Al_{13}Fe_4$	0	0.00446

The experimental results were confirmed by calculations performed using SOLGASMIX. This indicates that the reactions are forming the equilibrium compounds rather than intermediate compounds.

5.4 Chapter 5 Summary

Reactions for the Al-15mol% and Al-20mol% Fe_2O_3 samples could be initiated by mechanical alloying alone. There is an exponential relationship between the time of reaction and the charge ratio used during mechanical alloying. The exponential relationship develops because of changes in the number and energy of ball collisions during milling.

Thermal analysis combined with x-ray diffraction shows that the reactions in the Al-Fe_2O_3 system are a two step process where first, Fe_2O_3 is reduced to Fe_3O_4 and then, the Fe_3O_4 is reduced by Al to form $Al_{13}Fe_4$. Increased mechanical alloying time lowers the reaction temperature for the conversion of hematite to magnetite. The reduction in temperature is the result of increased surface area of reactant particles and increased diffusion via deformation induced short-circuit pathways.

The exothermic self-propagating reduction of magnetite to form $Al_{13}Fe_4$ is slowed by increased milling time. This may be due to increased heat dissipation for the isolated particles of a more uniformly distributed reactant mixture.

Thermodynamic calculations utilizing the SOLGASMIX-PV program indicate that the products formed during the reactions are the thermodynamically favored phases.

References

1. G. B. Schaffer, P. G. McCormick, Metall. Trans., 23A, 1992, pp. 1285-1290.
2. B. J. M. Aikin, T. H. Courtney, D. R. Maurice, Mater. Sci. and Eng., A147, 1991, pp. 229-237.
3. G. B. Schaffer, P. G. McCormick, Materials Forum, 16, 1992, pp. 91-97.
4. J. S. Forrester, G. B. Schaffer, Metall. and Mater. Trans., 26A, 1995, pp. 725-730.
5. B. E. Warren, *X-Ray Diffraction*, Dover, New York, 1990.
6. G. T. Hida, I. J. Lin, Combustion and Plasma Synthesis of High Temperature Materials, Ed. Z. A. Munir and J. B. Holt, VCH Pub., New York, 1990, pp. 246-261.
7. A. O. Aning, Z. Wang, T. H. Courtney, Acta Metall. Mater., 41, 1, 1993, pp. 165-174.
8. P. G. Boswell, J. of Thermal Analysis, 18, 1980, pp. 353-358.
9. L. Takacs, M. A. Susol, J. Sol. State Chem., 121, 2, 1996.
10. T. M. Besmann, SOLGASMIX-PV, Computer Program to Calculate Equilibrium Relationships in Complex Chemical Systems, Oak Ridge National Lab/TM-5775, 1977.
11. L. S. Darken and R. W. Gurry, Physical Chemistry of Metals, McGraw-Hill, New York, 1953, 349.

Chapter 6 Densified Sample Analysis: Results and Discussion

6.1. Pressed and Sintered Parts

Mixtures containing Al and 1.75 or 3.5mol % Fe_2O_3 were mechanically alloyed at a 6:1 charge ratio for times between 0.5 and 10 hrs. The mixtures were then heat treated at several temperatures for different times in argon to initiate displacement reactions and to study the reaction phase morphology and stability. Densified samples were produced by pressing powder in a 2.54 cm die at 620 MPa. Samples were then sintered in argon at 550°C for 1 hr.

6.1.1. Microscopy

Typical microstructures for the 1.75 mol% Fe_2O_3 mechanically alloyed powders prior to reaction are shown in Figs. 22 and 23. Similar microstructures were produced in the Al-3.5mol% Fe_2O_3. samples and are shown in Figs. 24 and 25. In all 4 figures, the light regions are primarily aluminum and the darker regions are rich in Fe_2O_3 particles. Figures 22 and 24 have a distinctive lamellar appearance which is typical for the early stages of mechanical alloying (MA). The structure develops as the result of repeated fracture and welding of the Al along with trapping of Fe_2O_3 particles in between the Al particles. As MA milling continues, the lamellar structure is eventually eliminated and a uniform distribution of Fe_2O_3 particles is created.

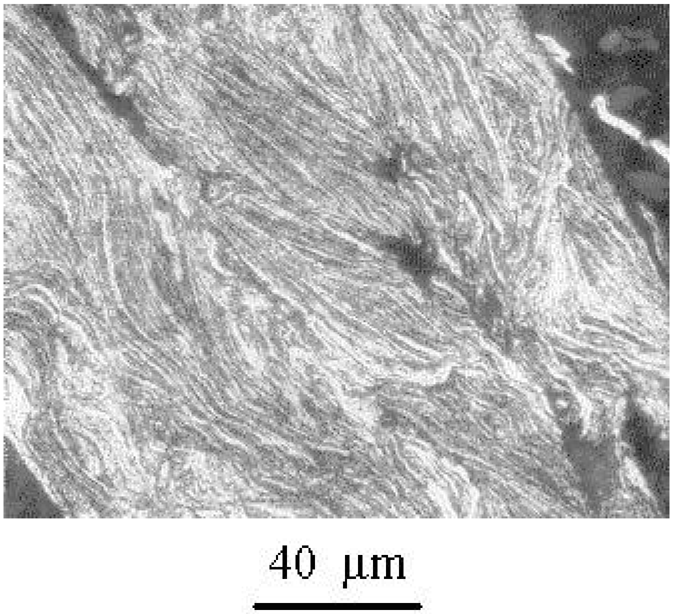

Fig. 22. Optical micrograph of Al-1.75mol% Fe_2O_3 after 1/2 mill

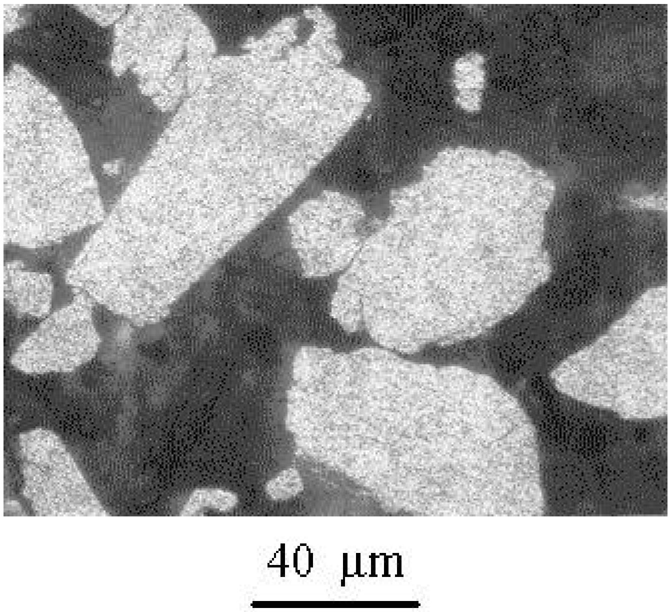

Fig. 23. Optical micrograph of Al-1.75mol% Fe_2O_3 after 5 hr mill

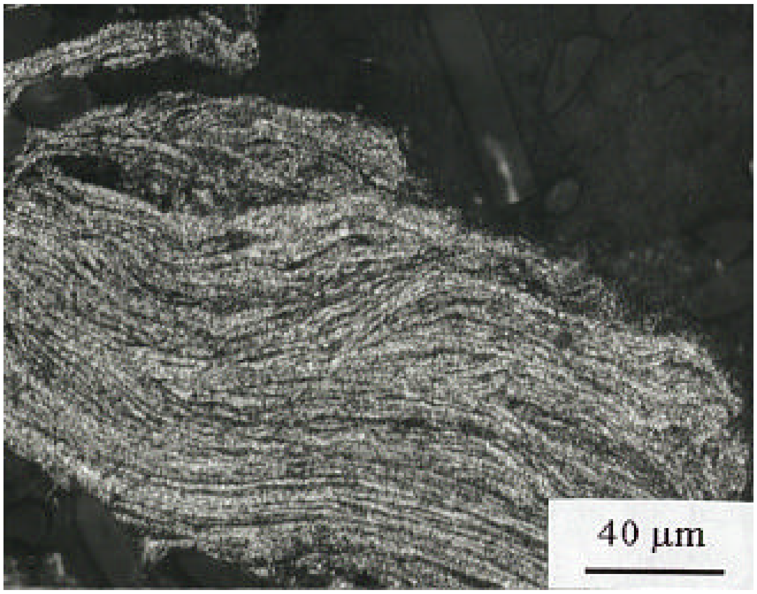

Fig. 24. Optical micrograph of Al-3.5mol% Fe_2O_3 after 1/2 hr mill

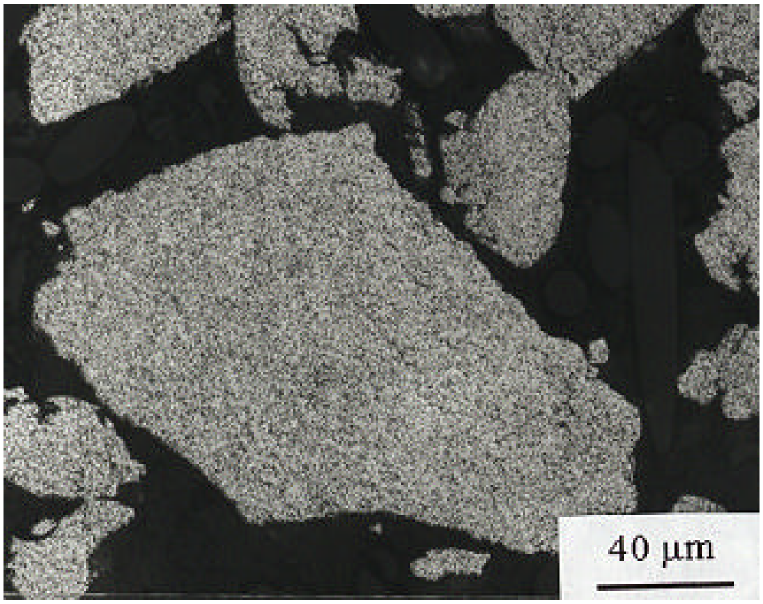

Fig. 25. Optical micrograph of Al-3.5mol% Fe_2O_3 after 5 hr mill

Although the increased milling time is markedly changing the microstructure of the powders, it is not affecting the Fe_2O_3 particle size. Figure 26 shows a plot of the Fe_2O_3 particle size as a function of milling time for Al - 3.5 mol% Fe_2O_3 samples. The 1/2 and 5hr sizes were determined from scanning electron microscope (SEM) images. The initial Fe_2O_3 particle size was determined using a laser light scattering particle size analyzer. Most of the reduction of Fe_2O_3 particle size has occurred in the first 1/2 hr of MA milling. The additional milling time is simply leading to a more uniform distribution of the starting materials.

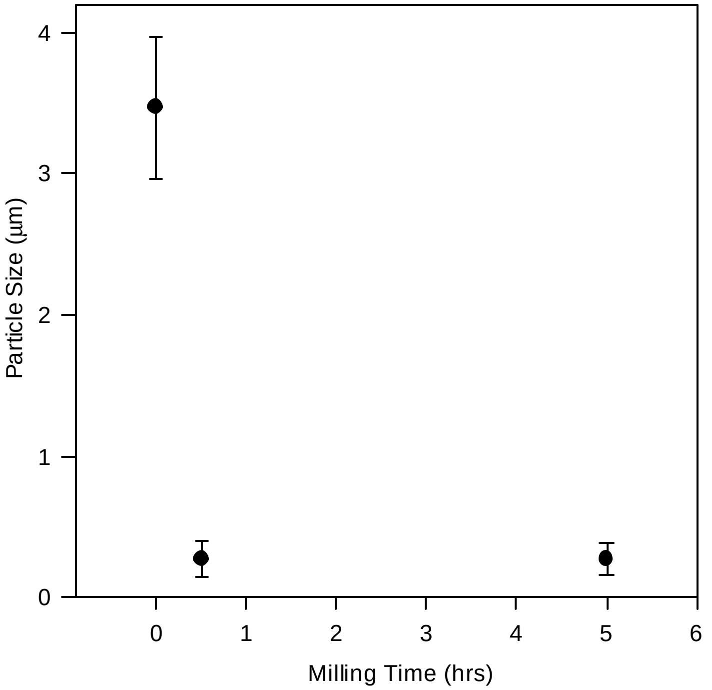

Fig. 26. Fe_2O_3 particle size for Al-3.5mol% Fe_2O_3 samples milled at 6:1 charge ratio for 1/2 and 5 hrs. The 1/2 and 5hr measurements were made from SEM micrographs. The 0 hr measurement was made using a laser light scattering particle size analyzer.

Following milling the pressed samples were heat treated to initiate reactions. Furnace temperatures and times were based on x-ray diffraction and differential thermal analysis (DTA) results. Paralleling the

DTA work, optical micrographs show that, after longer milling times, the displacement reaction to form $Al_{13}Fe_4$ seems to be impeded. An example of this is seen in Fig. 27, where Fig. 27a shows an Al - 3.5 mol% Fe_2O_3 - 1/2 hr milled sample which was heat treated at 500°C for 5 hrs and has reacted to form Al and $Al_{13}Fe_4$. Figure 27b shows a 3.5 mol% Fe_2O_3 - 5 hr mill sample which was heat treated along with the 1/2 hr mill sample. The micrograph and x-ray diffraction confirm Fe_3O_4 has been formed but no reaction to $Al_{13}Fe_4$ has occurred.

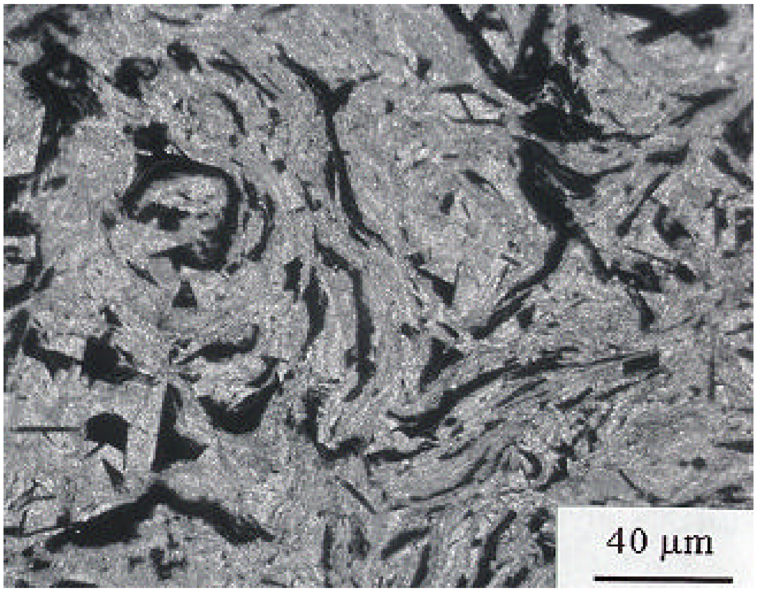

Fig. 27a. Optical micrograph of Al - 3.5 mol% Fe_2O_3 - 1/2 hr milled sample which was heat treated at 500°C for 5 hrs and has reacted to form Al and $Al_{13}Fe_4$.

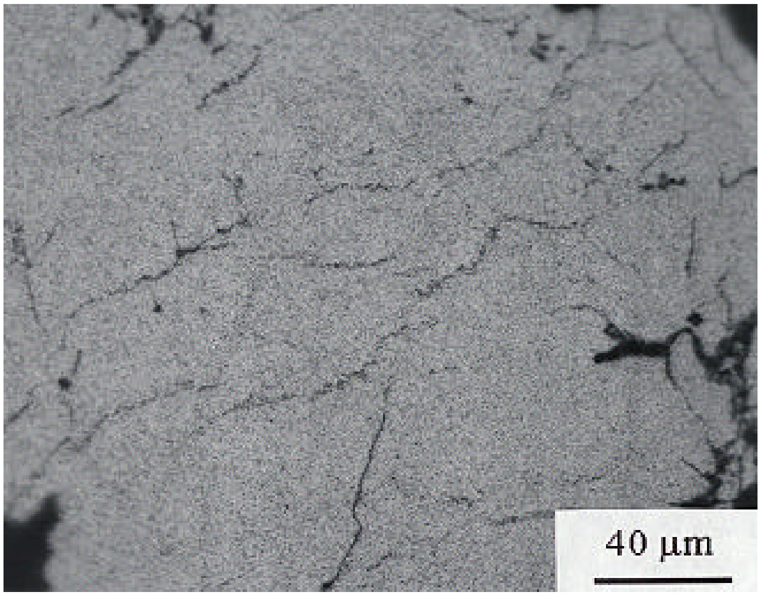

Fig. 27b. Optical micrograph of Al - 3.5 mol% Fe_2O_3 - 5 hr milled sample which was heat treated at 500°C for 5 hrs and has reacted to form Fe_3O_4 but not $Al_{13}Fe_4$.

Further heat treatments at 550°C for 5 hrs show the formation of $Al_{13}Fe_4$ in both the 1/2 hr and 5 hr milled samples. However, the reactant size in the 5hr sample is much smaller than the 1/2 hr sample, again indicating that the reaction is being inhibited in the 5 hr milled sample. Figures 28a and 28b show optical micrographs of the 1/2 hr and 5hr following that heat treatment.

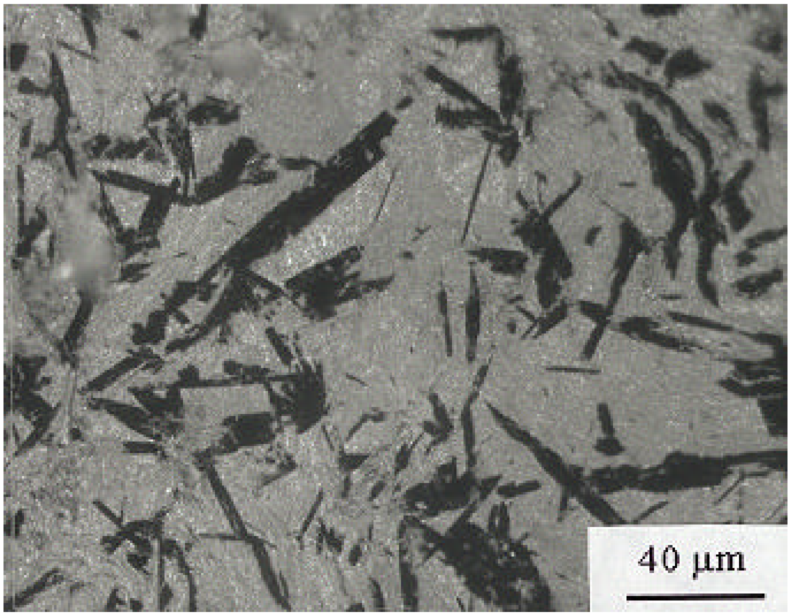

Fig. 28a. Optical micrograph of Al - 3.5 mol% Fe_2O_3 - 1/2 hr milled sample which was heat treated at 550°C for 5 hrs and has reacted to form $Al_{13}Fe_4$.

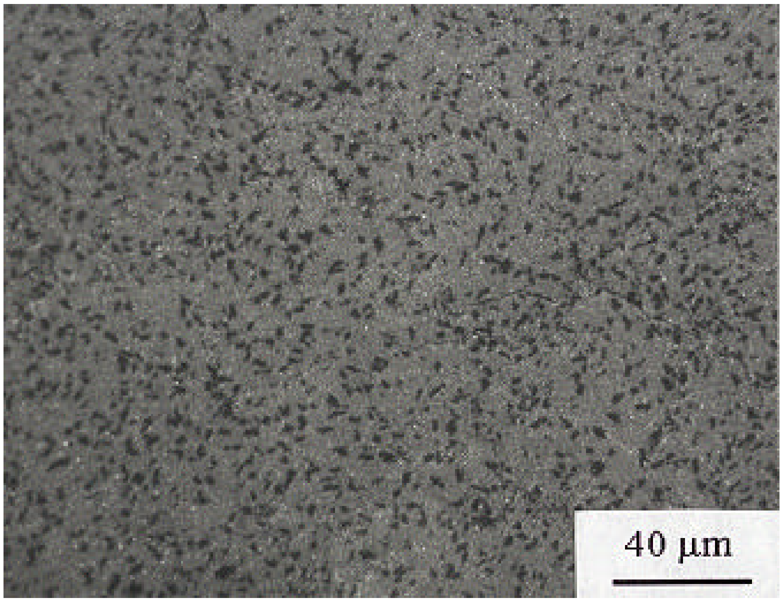

Fig. 28b. Optical micrograph of Al - 3.5 mol% Fe_2O_3 - 5 hr milled sample which was heat treated at 550°C for 5 hrs and has reacted to form $Al_{13}Fe_4$ but at much smaller size compared to the 1/2 hr milled sample.

The reduction in product particle size with increasing milling time levels off at about the same time at which a homogeneous mixture is produced. Figure 29 shows a plot of $Al_{13}Fe_4$ product size as a function of MA milling time. Samples were all heat treated together to 650°C at a heating rate of 20°C/min and then furnace cooled. The large deviation in particle sizes is a result of using a linear intercept method to measure a high aspect ratio particle.

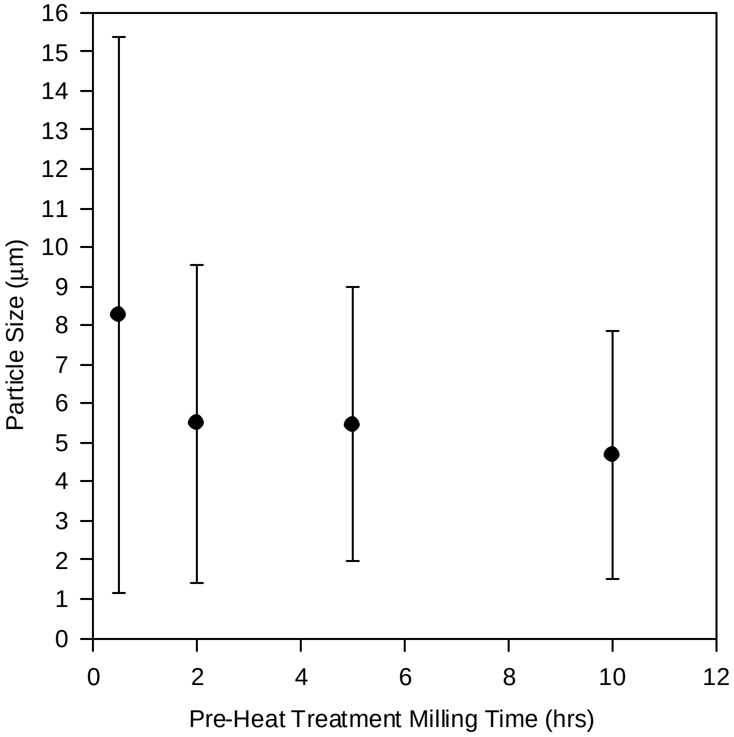

Fig. 29. Resultant $Al_{13}Fe_4$ particle size for Al-3.5mol% Fe_2O_3 samples following heat treatment at 650°C for 0 hrs.

Although the inhibition of the displacement reactions is not completely understood, the phenomenon was utilized to attempt to produce small (<2µm) incoherent particles to act as strengthening agents in the material. The Al-3.5mol% Fe_2O_3 -1/2 hr and 5hr - heat treated at 550°C for 5hr conditions were selected for further studies. Based on the optical micrographs shown in Fig. 28, average particle sizes, volume fractions and aspect ratios were measured and recorded in Table 9.

Table 9. Physical parameters for Al-3.5mol% samples determined from optical micrographs shown in Fig. 28.

	$Al_{13}Fe_4$ Particle Size (μm)	Volume Fraction (%)	Particle Aspect Ratio (l/t)
Al-3.5% 1/2 hr mill		0.29	8.2
Length	42.5±26.7		
Thickness	5.2±3.0		
Al-3.5% 5hr mill	2.8±0.5	0.30	~1

X-ray microprobe analysis was performed on the Al-3.5mol% Fe_2O_3 - 550°C 5hr sample to determine Al and Fe concentrations throughout the sample. Figure 30a shows Al concentrations with the color white being the highest concentration. The next highest concentration would be red with concentration decreasing through the visible spectrum down to violet. It can be seen that there is some gradient in the concentration around the formed particles. It is not simply a sharp drop at the $Al_{13}Fe_4$ phase boundaries.

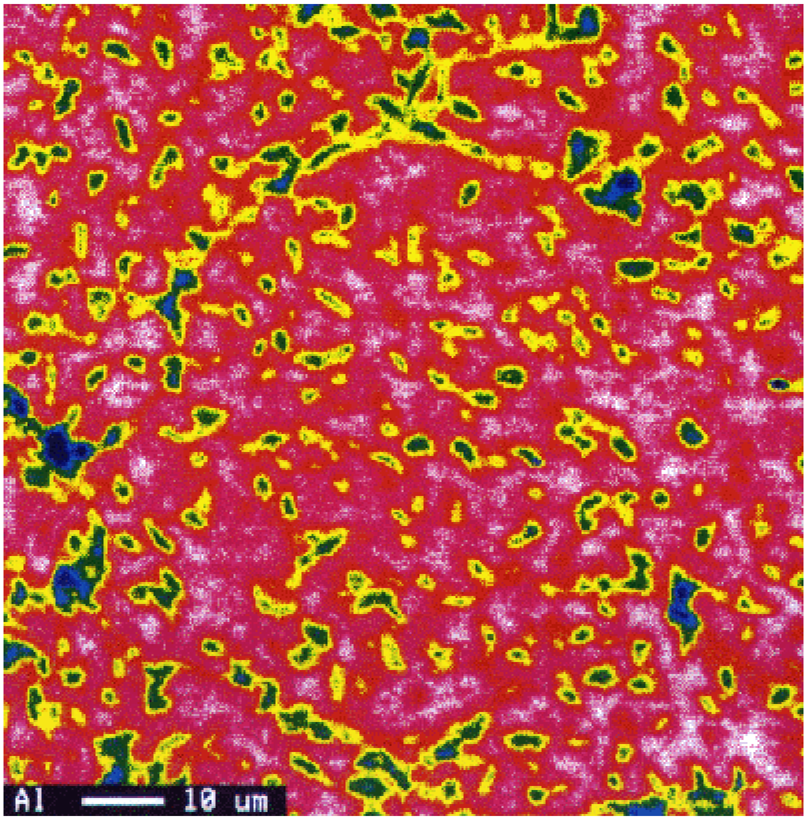

Fig. 30a X-ray microprobe map for Al in a Al-3.5mol% Fe_2O_3 5hr milled sample heat treated at 550°C for 5 hrs. Concentrations are highest at white and then red and then down through the visible spectrum to violet.

Figure 30b shows a similar x-ray map for iron concentrations. Again, there are similar gradients in the concentration with Fe content increasing towards the center of the particles. The gradient could be caused by a large sub-surface sampling volume of the incident electron beam. However, if a true gradient does exist, it shows that the reactions have not proceeded to completion.

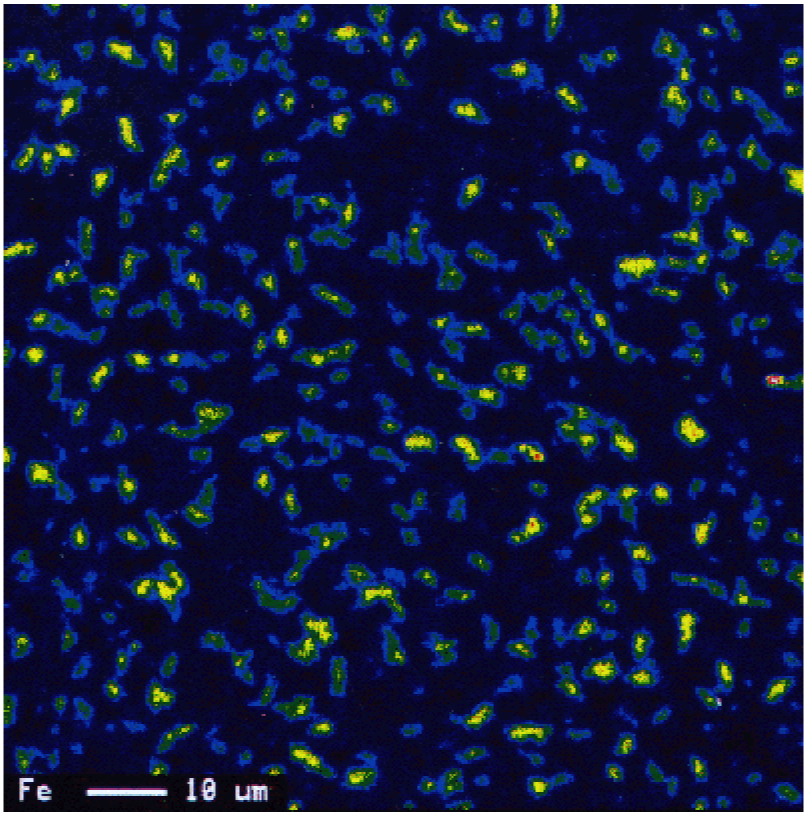

Fig. 30b X-ray microprobe map for Fe in a Al-3.5mol% Fe_2O_3 5hr milled sample heat treated at 550°C for 5 hrs. Concentrations are highest at white and then red and then down through the visible spectrum to violet.

Transmission electron microscopy (TEM) was performed on the Al-3.5mol% 1/2 hr and 5hr milled - 550°C 5hr samples. In Fig. 31a, the 1/2 hr milled sample shows light colored regions of Al separated by darker regions filled with small particles. In the 5 hr sample shown in Fig. 31b, the distribution of particles is more uniform. The more uniform distribution of particles should lead to higher strengths and hardnesses when considering an Orowan type strengthening model. Although electron diffraction was performed on the particles, they could not be readily indexed to the obvious possibilities of $Al_{13}Fe_4$ or Al_2O_3. At this point, it is only important that they are small incoherent particles.

Fig. 31a. TEM micrograph of Al-3.5mol% Fe_2O_3 - 1/2hr mill - heat treated at 550°C for 5 hrs.

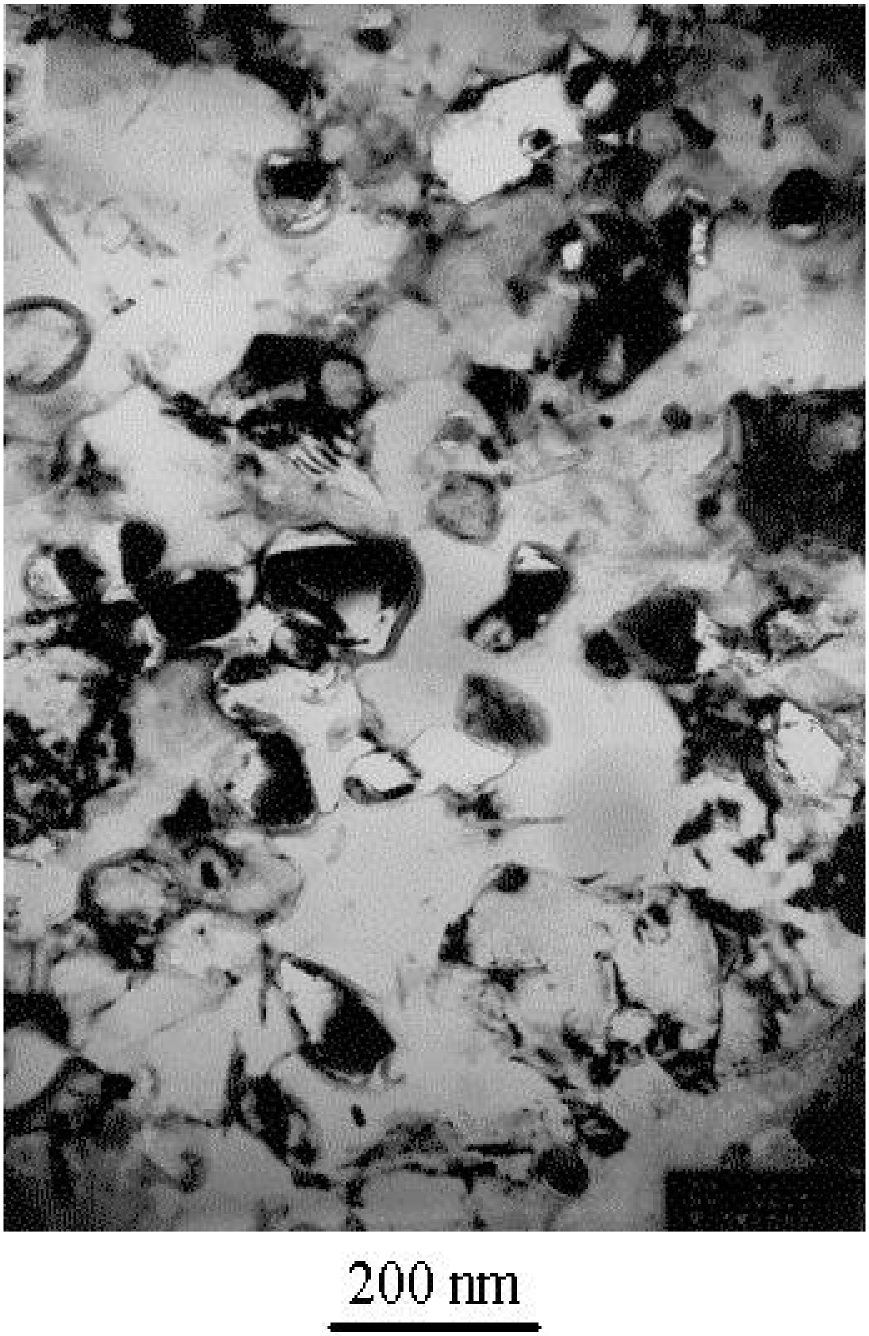

Fig. 31b TEM micrograph of Al-3.5 mol% Fe_2O_3 - 5hr mill - heat treated at 550°C for 5 hrs.

Rockwell hardness was performed on the pressed and sintered parts and recorded in Table 10. As expected from the TEM images, a significant increase in hardness was seen for the 5hr milled sample.

Table 10. Rockwell hardness values for the 3.5mol% pressed and sintered samples

	Rockwell Hardness (HRf)
3.5mol% Fe_2O_3 1/2hr	75.3±1.6
3.5mol% Fe_2O_3 5hr	82.0±3.9

6.2. Extruded Parts

Al-1.75mol% Fe_2O_3 1/2 hr mill and the Al-3.5mol% samples milled for 1/2 and 5 hours were reacted by annealing at 550°C for 5 hours. The Al-1.75mol% Fe_2O_3 5 hour milled sample had to be reacted at 600°C for 5 hours due to inhibition of the displacement reaction and failure to react at 550°C. The four powder samples were each encapsulated in 6061 aluminum cans. The cans were vacuum degassed at 500°C for 4 hours and extruded at 500°C with a 12:1 extrusion ratio. The Al-3.5mol% Fe_2O_3 1/2 hr mill sample did not extrude to form a uniform continuous extruded material. This may have been caused by the material itself, or simply an anomaly of the extrusion process. As a consequence, tensile results could not be obtained for this sample.

6.2.1. Microscopy

Scanning electron microscopy (SEM) using a backscatter electron (BSE) detector was used to analyze the microstructure of the 1.75 and 3.5 mol% extruded samples. Micrographs of the samples are shown in Figs. 32&33. Similar to the results from the pressed and sintered samples, the 3.5 mol% samples shown in Fig 32 have a marked decrease in particle size as a result of the increased milling time. Again, this can be attributed to the dissipation of heat away from reacting particles which suppresses the self-propagation of the reaction [1].

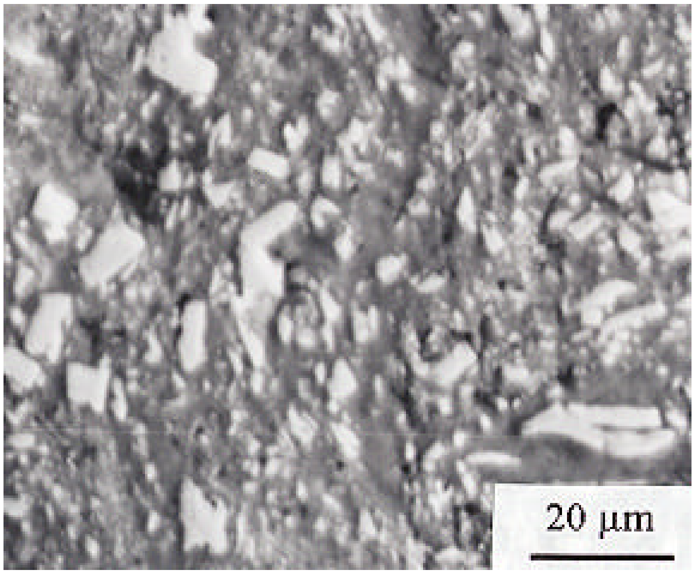

Fig. 32a. SEM BSE micrograph of Al-3.5mol% Fe_2O_3 1/2hr mill extruded sample

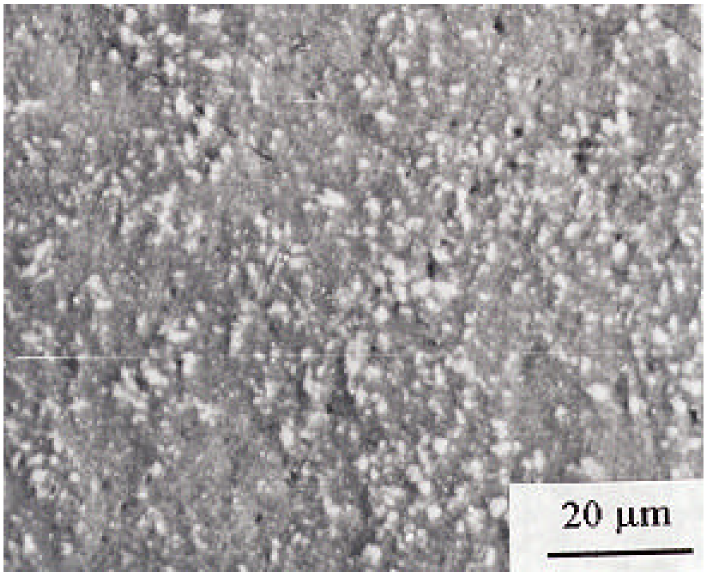

Fig. 32b. SEM BSE micrograph of Al-3.5mol% Fe_2O_3 5hr mill extruded sample

The Al - 1.75 mol% Fe_2O_3 samples differ slightly from the 3.5mol% samples. The 1/2hr mill sample shown in Fig 33a has large elongated $Al_{13}Fe_4$ particles which would be anticipated from the pre-reaction microstructure shown in Fig. 22. The 5 hr milled sample particles shown in Fig. 33b, however, seem larger and further spaced with a lower volume fraction than what would be anticipated. It is most likely the result of the increased temperature required to initiate reactions in this powder. Because of the inability to initiate reactions in the 1.75mol% 5 hr powders at 550°C, the powders were reacted at 600°C. At the elevated temperatures, the reacted particles will coarsen and be reduced in number leading to the appearance of a lower volume fraction.

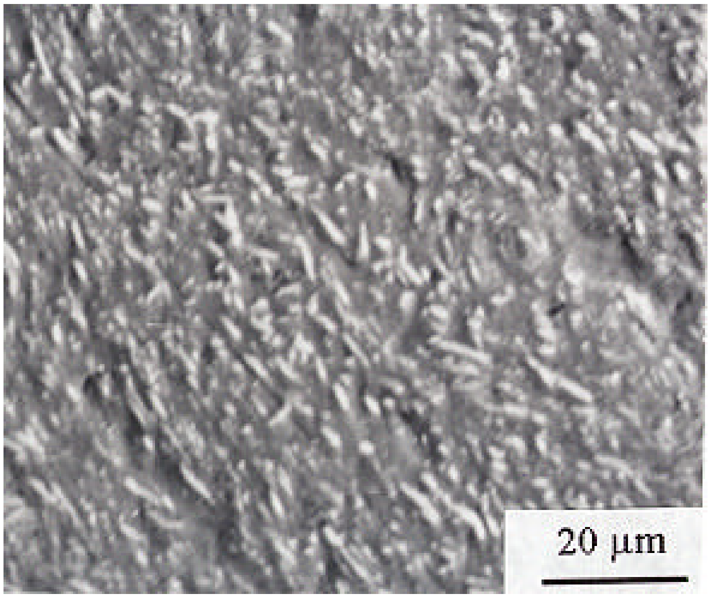

Fig. 33a. SEM BSE micrograph of Al-1.75mol% Fe_2O_3 1/2hr mill extruded sample

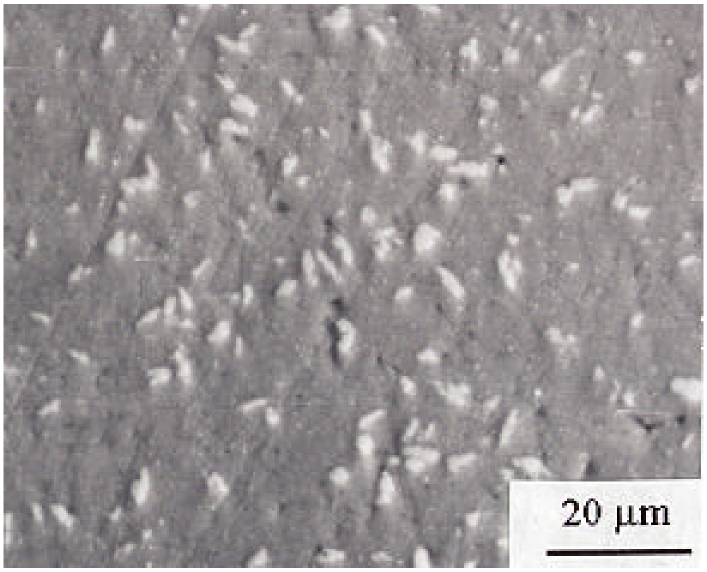

Fig. 33b. SEM BSE micrograph of Al-1.75mol% Fe_2O_3 5hr mill extruded sample

6.2.2. Density

Densities for the 4 extruded samples were determined using an archimedian measurement. The resulting values are recorded in Table 11.

Table 11. Density values for extruded samples

Sample	Density (g/cc)
Al - 1.75mol% Fe_2O_3 1/2 hr mill	2.81 ± 0.01
Al - 1.75mol% Fe_2O_3 5 hr mill	2.78 ± 0.01
Al - 3.5mol% Fe_2O_3 1/2 hr mill	2.77 ± 0.01
Al - 3.5mol% Fe_2O_3 5 hr mill	2.84 ± 0.01

Density value for pure Al = 2.70 g/cc

6.2.3. Mechanical Properties

Following extrusion, tensile specimens were machined such that the gage section revealed the powder metallurgy (P/M) section of the extrusion. This left the grip sections of the specimens as an exterior coating of the 6061 Al can surrounding the P/M material gage section. Because of the excellent bonding of the can to the P/M material and because an extensometer was used to determine strain values, it is believed that this sample arrangement had very little effect on the measured properties. Representative engineering stress-strain curves for the extruded samples are shown in Fig. 34. Average yield strength, ultimate tensile strength, Young's modulus, and elongation to failure values were determined from the tensile tests and are recorded in Table 12. Also included in Table 12 are Rockwell and Knoop hardness values measured on transverse sections of the extrusions.

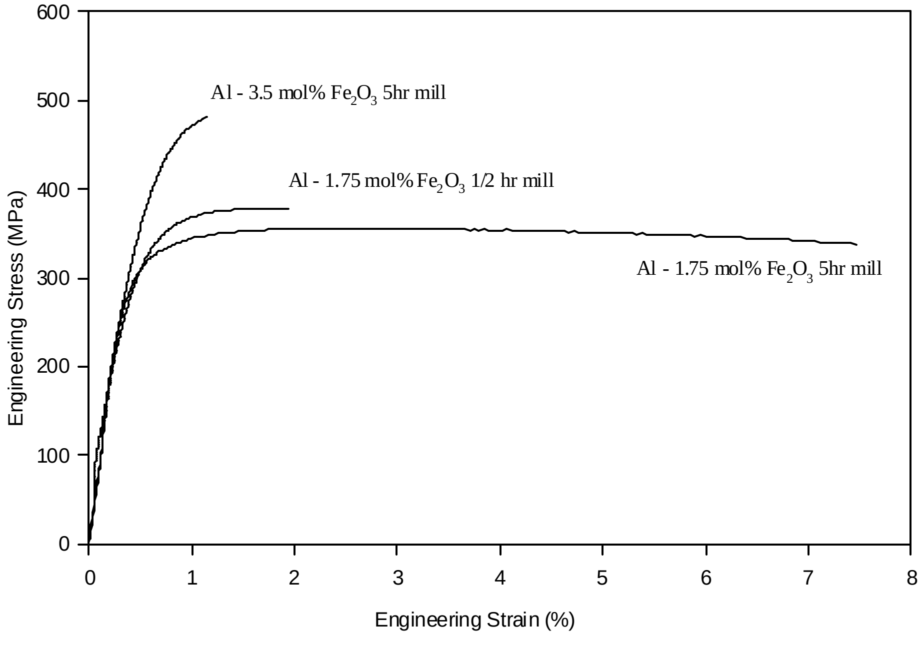

Fig. 34. Representative engineering stress-strain curves for tensile tests performed on extruded samples.

Table 12. Mechanical properties for extruded samples

Sample	Rockwell Hardness (HRa)	Knoop Hardness (HkN)	0.2% Yield Strength (MPa)	Ultimate Tensile Strength (MPa)	Young's Modulus (GPa)	Elongation (%)
Al - 1.75mol% Fe_2O_3 1/2 hr mill	39.1±1.3	125±6	340±2.8	374±6.4	51.2±2.4	1.7±0.4
Al - 1.75mol% Fe_2O_3 5 hr mill	39.6±0.4	117±3	325±4.2	354±2.9	59.5±6.0	6.6±1.3
Al - 3.5mol% Fe_2O_3 1/2 hr mill	41.1±0.6	116±6	-	-	-	-
Al - 3.5mol% Fe_2O_3 5 hr mill	48.9±0.3	152±3	433±10.6	457±35.0	65.5±0.6	1.0±0.3

From the SEM micrographs shown in Figs. 32 and 33, several key elements were measured and recorded in Table 13. These include the average particle size, volume fraction, and particle aspect ratio. From these value, estimates can be made for various strengthening mechanisms which may be present in the system.

Table 13. Values determined from SEM micrographs

	$Al_{13}Fe_4$ Particle Size (μm)	Volume Fraction	Particle Aspect Ratio (l/t)
Al-1.75% 1/2hr mill		0.21±0.08	4.2
Length	4.7±2.1		
Thickness	1.1±0.2		
Al-1.75% 5hr mill	2.0±0.9	0.13±0.08	~1
Al-3.5% 1/2 hr mill		0.31±0.09	2.7
Length	8.9±4.9		
Thickness	3.3±1.2		
Al-3.5% 5hr mill	1.6±0.5	0.33±0.13	~1

Based on the observed microstructures, the materials seem to behave in a manner consistent with current strengthening theories. Using the Ashby-Orowan equation (Eq. 2.8)[2], the Ashby-Orowan-Kelly equation (Eq. 2.10)[3], and an equation for critical resolved shear stress (Eq. 6.1) shown below, estimates were made and recorded in Table 6 on the effects of the large $Al_{13}Fe_4$ particles and smaller particles seen during TEM on the yield strength of the material as it relates to incoherent particles.

$$\Delta s = M\Delta t \tag{6.1}$$

In Eq. 6.1, Ds the increase in the applied stress, Dt is the increase in the resolved shear stress, and M is the Taylor factor (reciprocal of the Schmid factor) which for an FCC polycrystal has been estimated to be M = 3.1 [4]. Also included in Table 6 are calculated values for strength effects from differences in thermal expansion based on the equations of Arsenault [5].

Table 14. Possible contributions to strength increase between 3.5 mol% 1/2 hr and 5 hr milled samples

Mechanism	Estimated Contribution to Strength Increase			
	1.75% 1/2hr	1.75% 5hr	3.5% 1/2hr	3.5% 5hr
Incoherent Particles (Orowan)				
$Al_{13}Fe_4$	11.8 MPa	9.6 Mpa	7.1 Mpa	24.5 Mpa
TEM Particles	-	-	Minimal	76 MPa
Enhanced Work Hardening (Composite)				
ΔCTE	2.0 MPa	1.4 MPa	1.7 MPa	2.8 MPa
Grain Size/Subgrain Size	Minimal	Minimal	Minimal	Minimal
Solid Solution Strengthening				
Fe in Al	Minimal	Minimal	Minimal	Minimal
O in Al	Minimal	Minimal	Minimal	Minimal
Work Hardening	Minimal	Minimal	Minimal	Minimal

Based on these estimates, several conclusions can be drawn. Foremost, at their current size, the reaction product particles ($Al_{13}Fe_4$) will have limited impact on the overall strength of the materials. Also, looking at the 3.5 mol% samples and the limited mechanical properties, it seems that increased MA milling time is leading to higher hardness values and this would in turn mean higher strengths. Based on the results of Table 14, the higher hardness values are likely the result of the fine incoherent particles seen in the TEM micrographs.

6.2.4. Chemical Analysis

Results from chemical analysis are shown in Table 15. Chemical analysis was performed as a means to evaluate chemical contamination from the ball milling process and process control agents. Because the concentrations of Cr are below detectable levels, it is believed that contamination from the stainless steel milling media is minimal.

Table 15. Chemical analysis results for extruded samples

Element	Al - 1.75mol% Fe_2O_3 6:1 1/2 hr (wt%)	Al - 1.75mol% Fe_2O_3 6:1 5 hr (wt%)	Al - 3.5 mol% Fe_2O_3 6:1 5 hr (wt%)
Al	Balance	Balance	Balance
Fe	4.65±0.09	4.46±0.09	9.72±0.19
Si	0.24±0.01	0.130	0.14
Ni	0.07	0.16	0.08
Pb	0.05	0.04	0.05
Sn	0.03	0.03	0.03
Cr	<0.01	<0.01	<0.01

6.2.5. Particle Coarsening Analysis

If it is assumed that the $Al_{13}Fe_4$ particles are forming and then growing to some size an evaluation of their coarsening behavior may yield valuable information for future work. Based on the coarsening rate, an estimate of the initial particle size can be made. From that size, estimates on the strengthening behavior can be determined. Figure 35 shows the $Al_{13}Fe_4$ particle size as a function of time at 550°C. Based on linear extrapolation of Figure 35, it appears that the finest particles that could be formed are in the 2 µm range, not much different from the 3 µm particles obtained for 5hrs at 550°C in the pressed and sintered samples.

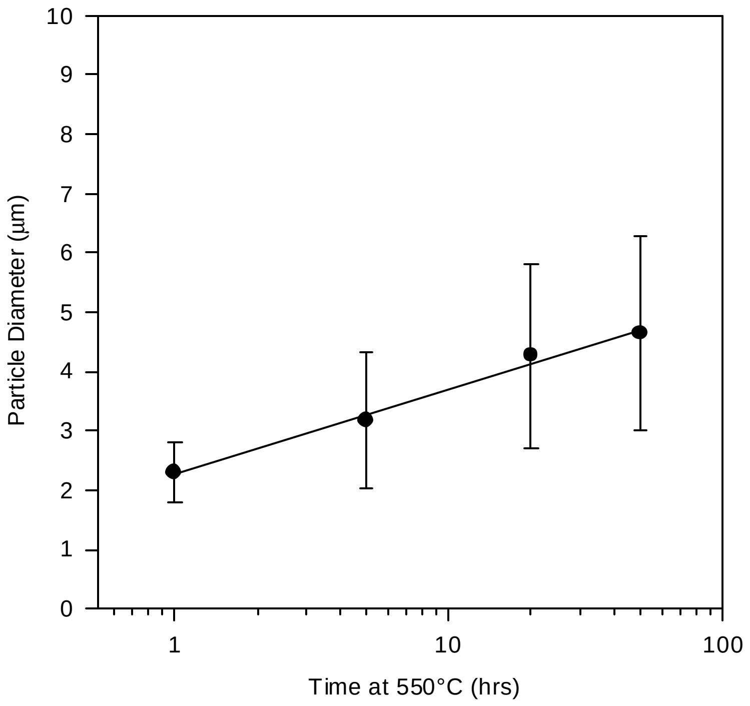

Fig. 35. $Al_{13}Fe_4$ particle size for Al-3.5mol% Fe_2O_3 6:1 5hr milled samples heat treated at 550°C for various times.

6.3. Chapter 6 Summary

Microstructural evidence confirms that the chemical reaction forming $Al_{13}Fe_4$ was being inhibited by increased MA milling time. As a result, finer, more uniformly distributed particles were formed. These particles, as well as particles revealed during TEM analysis were most likely the reason for increased mechanical properties in the 3.5mol% samples. A similar trend was not seen in the 1.75mol% samples because the samples did not respond to heat treatments in a similar manner. This again was attributed to the inhibited chemical reactions.

In the Al-3.5mol% Fe_2O_3 system, linear extrapolation indicated that the minimum $Al_{13}Fe_4$ product particle size would be in the range of 2 µm. Particles of this size would provide some amount of strengthening (~20 Mpa), however, the dramatic reduction of particle size as a result of mechanical alloying was of primary interest. Increased MA milling time lead to the reduction in the $Al_{13}Fe_4$ product particle size. The smaller particle size resulted from the dissipation of heat away from reacting particles which suppressed the displacement reaction.

Fine incoherent particles as seen in TEM images were responsible for most of the strength and hardness increases observed in the Al-3.5 mol% Fe_2O_3 – 5hr mill alloy.

The room temperature mechanical properties of the 1.75mol% 5 hr mill sample were comparable to or better than many 3000 or 5000 series aluminum alloys. Table 16 shows a comparison of several of these alloys against the 1.75mol% 5 hr mill sample.

Table 16 Comparison of several aluminum alloys

Alloy	Temper Condition	0.2% Yield Strength (MPa)	Ultimate Tensile Strength (MPa)	Elongation to Failure (%)
Al – 1.75mol% Fe_2O_3		325	354	7
3003	H18	186	200	4
3004	H38	248	283	5
5083	H343	283	359	8
5456	H343	297	386	8

References

1. L. Takacs, M. A. Susol, J. Sol. State Chem., 121, 2, 1996.
2. M. F. Ashby, Proc. 2nd Bolton Landing on Oxide Dispersion Strengthening, Ed. G. S. Ansell, T. D. Cooper, F. V. Lenel, Gordon Breach, New York, 1968, pp. 143-209.
3. P. M. Kelley, Int. Metall. Rev., 18, 1973, pp. 31-36.
4. G. E. Dieter, Mechanical Metallurgy, 3rd Edition, McGraw-Hill, New York, 1986, pp. 188-189.
5. R. J. Arsenault, Composite Structures 4, vol. 2, Applied Sci. Pub., 1987, pp. 2.70-2.81

Chapter 7 Conclusions

Reactions for the Al-15mol% and Al-20mol% Fe_2O_3 samples could be initiated by mechanical alloying alone. There was an exponential relationship between the reaction initiation time and the charge ratio used during mechanical alloying. The charge ratio is a reflection of energy input in the form of number and intensity of collisions occurring during the milling.

Thermal analysis combined with x-ray diffraction showed that the reactions in the Al-Fe_2O_3 system were a two step process where first, Fe_2O_3 (hematite)was reduced to Fe_3O_4 (magnetite) and then, Fe_3O_4 was reduced by Al to form $Al_{13}Fe_4$. Increased mechanical alloying time lowered the reaction temperature for the conversion of hematite to magnetite. The reduction in the reaction initiation temperature was the result of increased surface area of the reactant particles and increased diffusion via deformation induced short-circuit pathways.

The exothermic self-propagating reduction of magnetite to form $Al_{13}Fe_4$ was slowed by increased milling time. This may be due to increased heat dissipation from the isolated particles of a more uniformly distributed reactant mixture. Microstructural evidence confirms that the displacement reaction was being inhibited by increased MA milling time. As a result, a finer and more uniformly distributed particles were formed. These particles, as well as particles revealed during TEM analysis were responsible for increased mechanical properties in the 3.5mol% samples. A similar trend was not seen in the 1.75 mol% samples because the samples did not respond to heat treatments in a similar manner. This again is attributed to the inhibited displacement reactions.

Increased MA milling time led to the reduction in the product particle size. In the Al-Fe_2O_3 system, the minimum product particle size was in the range of 1-2 μm. Particles of this size will provide some amount of strengthening (~20 MPa), however, the dramatic reduction of the $Al_{13}Fe_4$ product particle size as a result of mechanical alloying was of great significance.

The room temperature properties of the 1.75mol% Fe_2O_3 – 5hr mill sample are comparable to many 3000 and 5000 series aluminum alloys. Should an alloy with this strength maintain those strengths at elevated temperatures, it would show great promise for many applications.

Chapter 8 Future Work

Mechanical Alloying and Chemical Reactions

Numerous studies have been undertaken to understand the mechanics and physics of mechanical alloying with respect to metal-metal alloying and dispersion strengthening. Very little, however, has been done on understanding the effects of MA on chemical reactions. Based on the initial work accomplished here, a relationship could be developed between energy input (charge ratio) and the effect on reaction kinetics. As a result, predictions could then be made on the effects of mechanical alloying on a variety of other reaction systems. The work could be expanded to include other aspects of mechanical alloying such as variations in milling temperature, milling equipment, and pre-reaction particle distribution. Including these other variations would further expand and solidify the knowledge of the kinetics of MA.

Increased MA milling time resulted in a more uniform distribution of reactant particles. The resulting product particles were also more uniformly distributed. At the same time, the reaction temperature of the powder mixtures increased with milling time. This effect was attributed to heat dissipation into the isolated reacting particle surroundings. Other material systems could also benefit from this type of occurrence. Calculations to determine thermal conductivity with respect to volume fraction, particle size, and spacing would be helpful in determining the necessary parameters of a precursor mixture.

High Temperature Aluminum Alloys

The room temperature mechanical properties of the Al-1.75mol% Fe_2O_3 sample showed great promise for continued work with this system. However, future work must incorporate the ability to achieve finer reaction particle sizes to more strongly enhance strength and allow for a better chance to achieve high temperature strength. In the current work, the formed particles were unstable at elevated temperatures and rapidly coarsened. Modifications to the alloy chemistry may aid in maintaining particle stability. In addition, it would be of interest to study a system where the reaction product would be more resistant to particle coarsening. This includes the Al-Si-Fe-V system and also systems which would form stable ceramic particles or carbides such as Al-Si-C, Al-Ti-C, or Al-C.

Vita

Michael Thomas Stawovy was born on September 22, 1969 in Pittsburgh, Pennsylvania. He is the fifth of six children born to Theodore and Frances Stawovy. He was raised in the rural community of Belle Vernon, Pennsylvania approximately 30 miles south of Pittsburgh. In the summer of 1991, he completed the requirements for a Bachelor of Science in Materials Engineering from Virginia Tech. In the fall of 1994, he completed the requirements for a Masters of Science in Materials Science and Engineering also from Virginia Tech. In the summer of 1997, prior to completion of his doctoral degree, he took a position as a Senior Project Engineer for Advanced Technology with Aerojet Ordnance Tennessee (AOT) in Jonesborough, Tennessee. His current work focuses on research and development of refractory metal processing and properties. Because of his recent experience at AOT, he is considered to be an authority in the fields of liquid-phase and solid-state sintering, metalworking, near-net-shaping, and heat treating of refractory metals including tantalum, rhenium, molybdenum, tungsten and their alloys. His only future objective is to continue to educate himself in a variety of fields. These fields include materials science, agriculture, art, music, history, philosophy, family, and life.